Bioactive Materials 36 (2024) 358–375

Contents lists available at ScienceDirect

Bioactive Materials

journal homepage: www.keaipublishing.com/en/journals/bioactive-materials

Functional meniscus reconstruction with biological and biomechanical heterogeneities through topological self-induction of stem cells

Mingze Du [a,1], Kangze Liu [d,1], Huinan Lai [c,1], Jin Qian [c], Liya Ai [a], Jiying Zhang [a], Jun Yin [b,**], Dong Jiang [a,*]

[a] Department of Sports Medicine, Peking University Third Hospital, Institute of Sports Medicine of Peking University, Beijing Key Laboratory of Sports Injuries, Engineering Research Center of Sports Trauma Treatment Technology and Devices, Ministry of Education, Beijing, China
[b] The State Key Laboratory of Fluid Power Transmission and Control Systems, Key Laboratory of 3D Printing Process and Equipment of Zhejiang Province, School of Mechanical Engineering, Zhejiang University, Zhejiang, 310058, China
[c] Department of Engineering Mechanics, Key Laboratory of Soft Machines and Smart Devices of Zhejiang Province, Zhejiang University, Zhejiang, 310058, China
[d] School of Chemistry, Chemical Engineering and Biotechnology, Nanyang Technological University, 639798, Singapore

ARTICLE INFO

Keywords:
Tissue-engineered meniscus
Functional reconstruction
Mesenchymal stem cells
Heterogeneity
Topology structure

ABSTRACT

Meniscus injury is one of the most common sports injuries within the knee joint, which is also a crucial pathogenic factor for osteoarthritis (OA). The current meniscus substitution products are far from able to restore meniscal biofunctions due to the inability to reconstruct the gradient heterogeneity of natural meniscus from biological and biomechanical perspectives. Here, inspired by the topology self-induced effect and native meniscus microstructure, we present an innovative tissue-engineered meniscus (TEM) with a unique gradient-sized diamond-pored microstructure (GSDP-TEM) through dual-stage temperature control 3D-printing system based on the mechanical/biocompatibility compatible high M_w poly(ε-caprolactone) (PCL). Biologically, the unique gradient microtopology allows the seeded mesenchymal stem cells with spatially heterogeneous differentiation, triggering gradient transition of the extracellular matrix (ECM) from the inside out. Biomechanically, GSDP-TEM presents excellent circumferential tensile modulus and load transmission ability similar to the natural meniscus. After implantation in rabbit knee, GSDP-TEM induces the regeneration of biomimetic heterogeneous neomeniscus and efficiently alleviates joint degeneration. This study provides an innovative strategy for functional meniscus reconstruction. Topological self-induced cell differentiation and biomechanical property also provides a simple and effective solution for other complex heterogeneous structure reconstructions in the human body and possesses high clinical translational potential.

1. Introduction

The meniscus is a fibrocartilage tissue in the human knee joint that performs vital biofunctions, including load transmission, shock absorption, and maintaining knee stability, and contributes to joint lubrication. Meniscal injury can lead to osteoarthritis (OA) due to the destruction of natural biomechanics [1,2]. The biofunctions of the meniscus, especially buffering shock and absorbing stress, are accomplished through the synergetic effect of biological and biomechanical heterogeneities. The cell phenotype and extracellular matrix (ECM) deposition that progressively transit according to topographic localization, along with the orchestration of aligned collagen fibres, enable the meniscus to adequately distribute and absorb axial load under body weight, thus protecting the articular cartilage and attenuating joint degeneration [3]. Due to limited blood supply and structural specificity, the meniscus is difficult to self-repair after injury. Thus, meniscectomy is inevitable for severe meniscus tears and serves as the number one orthopaedic surgery in the US (approximately 700,000 cases every year)

Peer review under responsibility of KeAi Communications Co., Ltd.
* Corresponding author. Department of Sports Medicine, Peking University Third Hospital, Institute of Sports Medicine of Peking University, Beijing Key Laboratory of Sports Injuries, Engineering Research Center of Sports Trauma Treatment Technology and Devices, Ministry of Education, Beijing, China.
** Corresponding author. The State Key Laboratory of Fluid Power Transmission and Control Systems, Key Laboratory of 3D Printing Process and Equipment of Zhejiang Province, School of Mechanical Engineering, Zhejiang University, Zhejiang, 310058, China.
E-mail addresses: junyin@zju.edu.cn (J. Yin), bysyjiangdong@126.com (D. Jiang).
[1] These authors contributed equally to this work.

https://doi.org/10.1016/j.bioactmat.2024.03.005
Received 31 July 2023; Received in revised form 14 February 2024; Accepted 4 March 2024

[4]. Meniscectomy disrupts joint mechanics, leading to joint instability and OA development [5], which causes miserable suffering for a vast number of patients [6,7]. Therefore, meniscal biofunction restoration through meniscus substitute therapy is critical for allowing patients to return to sports and attenuating joint degeneration.

Tissue-engineered meniscus (TEM) application is currently the most promising strategy for inducing meniscal regeneration [8,9]. The greatest challenge of TEM application is biofunction restoration within the knee joint, which requires the concurrent reconstruction of the meniscus's gradient transitional biological and biomechanical hetero-structure. Attempts have been made to conceptually divide the meniscus into inner and outer zones and equip the two sections with different biomaterials, stem cells combined with regional-specific cytokines, decellularized meniscus ECM, and bioactive hydrogels [10–13]. However, these assemblies are distinctly zoned, lack flexibility and gradient transitions, which is not consistent with the natural meniscus, so that gradient transitions of the natural meniscus cell phenotype, ECM deposition and fibre alignments could not be implemented. Therefore, these assemblies failed to fully restore natural meniscus biofunctions or attenuate OA progression. Moreover, most of the corresponding methods are technically complex, which is not conducive to clinical translation. Besides, previously reported TEM original materials were hard to balance the biomechanical and biocompatible property due to the high-quality requirements of functional meniscus reconstruction [14].

The previous research on the effects of pore size on cell proliferation and differentiation showed that smaller pore size (100–250 μm) can induce more chondrogenic differentiation and facilitate cartilage-like matrix formation [15–17], while larger pore size (250–500 μm) can induce fibrogenic differentiation and facilitate fibrocartilage-like matrix formation [16,18,19]. Cells in the scaffold with smaller pore size appeared more rounded in shape, while cells in the scaffold with smaller pore size appeared more oval and fusiform-like in phenotype [16]. Nevertheless, differential differentiation of cells induced by different pore sizes on the same scaffold remains a challenge, which could be a novel idea for heterogeneous structural reconstruction of the natural meniscus. In the present study, we designed this heterogeneous scaffold through 3D printing with diamond-shaped pores gradient-sized from the inside out. Under the synergistic effect of bio-factors, the unique structure with spatially gradient-sized diamond pores was supposed to induce seeded bone marrow mesenchymal stem cells (BMSCs) to transitionally differentiate into different chondrocyte phenotypes. These

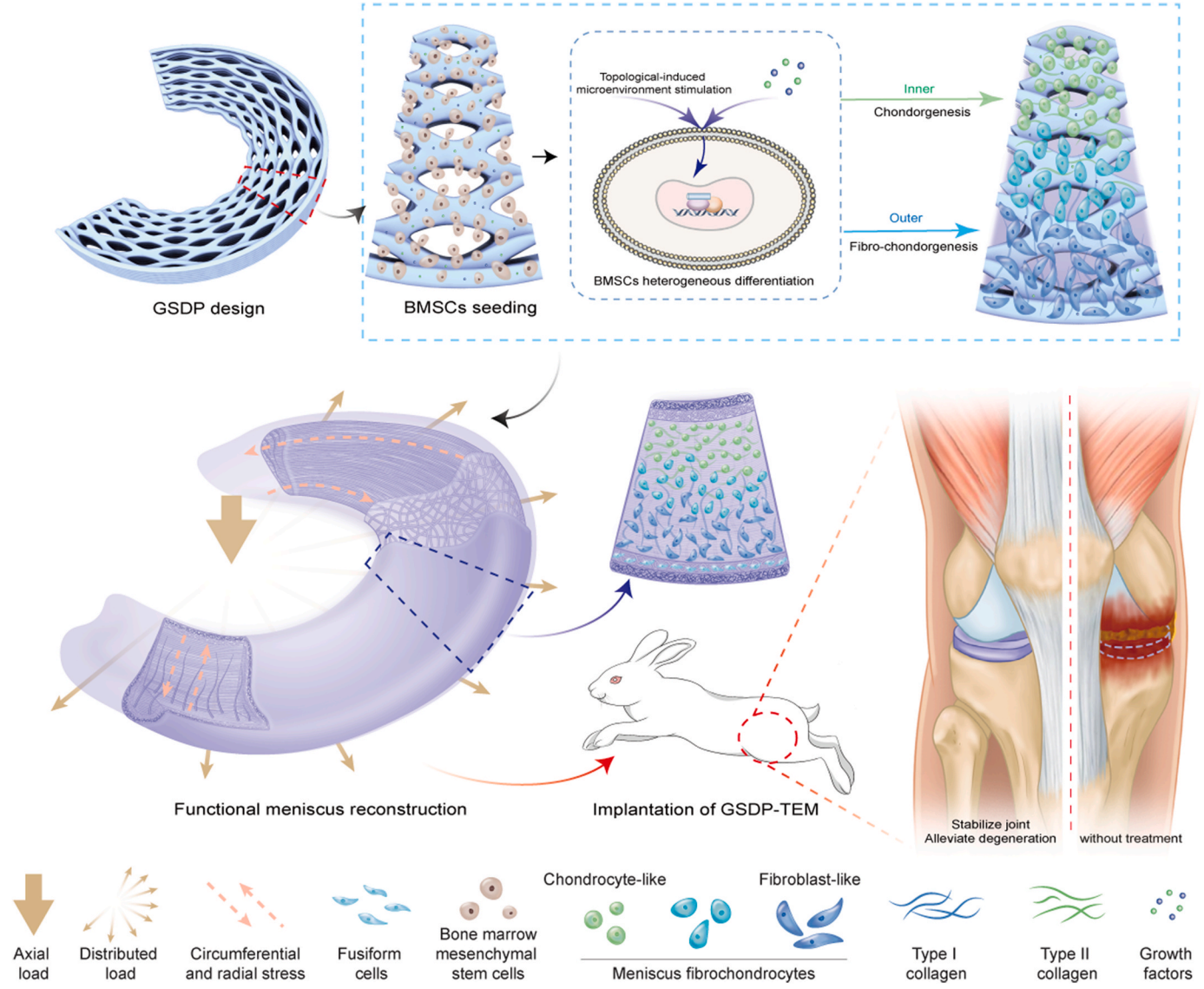

Fig. 1. Schematic of the present study. The 3D-printed TEM with a unique gradient-sized diamond-pored microstructure (GSDP-TEM) induces the reconstruction of biomimetic functional heterogeneous neomeniscus.

site-appropriate chondrocytes can secrete corresponding site-specific ECM to restore the natural meniscus's stress absorption and transmission functions. Thus, the biological heterogeneity was reconstructed. Moreover, the crescent-shaped wedge-like scaffold should possess excellent mechanical properties with biomimetic fibre alignment, achieving natural meniscus biomechanical function even before complete neomeniscus regeneration. In terms of the original materials, molecular etched PCL with high M_w was selected to endow the TEM with superior mechanical and biocompatible properties. With the synergetic effect of gradient-transiting biological and biomechanical heterogeneity mimicking the natural meniscus, this 3D-printed TEM with a unique gradient-sized diamond-pored microstructure (GSDP-TEM) could realize chondroprotection biofunctions and significantly attenuate cartilage degeneration after implantation into the rabbit knee joint (Fig. 1). This study might provide an innovative solution for artificial meniscus construction, combining biological and mechanical bionics with strong clinical translation potential. This study could also provide a simple and practical strategy for the challenging problem of reconstructing other complex heterogeneous tissues in the human body.

2. Materials and methods

2.1. Fabrication of the PCL scaffold

A 2/3 wedge-shaped disc meniscus scaffold was fabricated by fused deposition model 3D printing according to the native size of rabbit meniscus and our previous research [13]. The height of the inner ring of the wedge-shaped disc is 0.3 mm, the height of the outer ring is 1.5 mm, the diameter of the inner ring is 4 mm and the diameter of the outer ring is 10 mm. The mean pore size of the uniform square (USSP)-structured PCL scaffold was 215 μm. The PCL scaffolds with uniform diamond (USDP) -structured followed the rhombic short diagonal 158 μm for printing, and the short diagonal of the gradient diamond (GSDP) -structured PCL scaffold was 150 μm–350 μm from inside to outside (Figure S1). PCL (Daigang Bioengineering Co., Ltd., Shandong, China. M_w 150,000) was melted in the 3D printing nozzle and then 3D printed according to the path designed before. The printing system includes 3D communication, a stepping platform (gxyz303020vp, Zuo Youxin Intelligent Equipment Co., Ltd., Shandong, China), a pneumatic extrusion system, and a temperature control system. The working software repeater host v2 1.6 controls the two-stage heating block, and 3D_Print software controls the movement of the nozzle and platform.

For 3D printing of the designed scaffolds, PCL pellets were preheated inside the high-temperature extrusion printhead cartridge to allow for polymer melting and stabilization. Next, the scaffolds were 3D printed using an internal nozzle at a constant extrusion pressure. During the printing process layer-by-layer, the nozzle could lay down the PCL strands in the 0°–90° direction controlled by the computer-aided system. The computer-aided system is mainly the software that can control the motion of axes, which is written by ourselves with C++. When importing and running G-code containing movement coordinates, the program controls the movement of the axes so that the printhead can move to the predetermined position of the G-code. The printing parameters were set to ensure the homogeneous dispersion of the scaffolds'

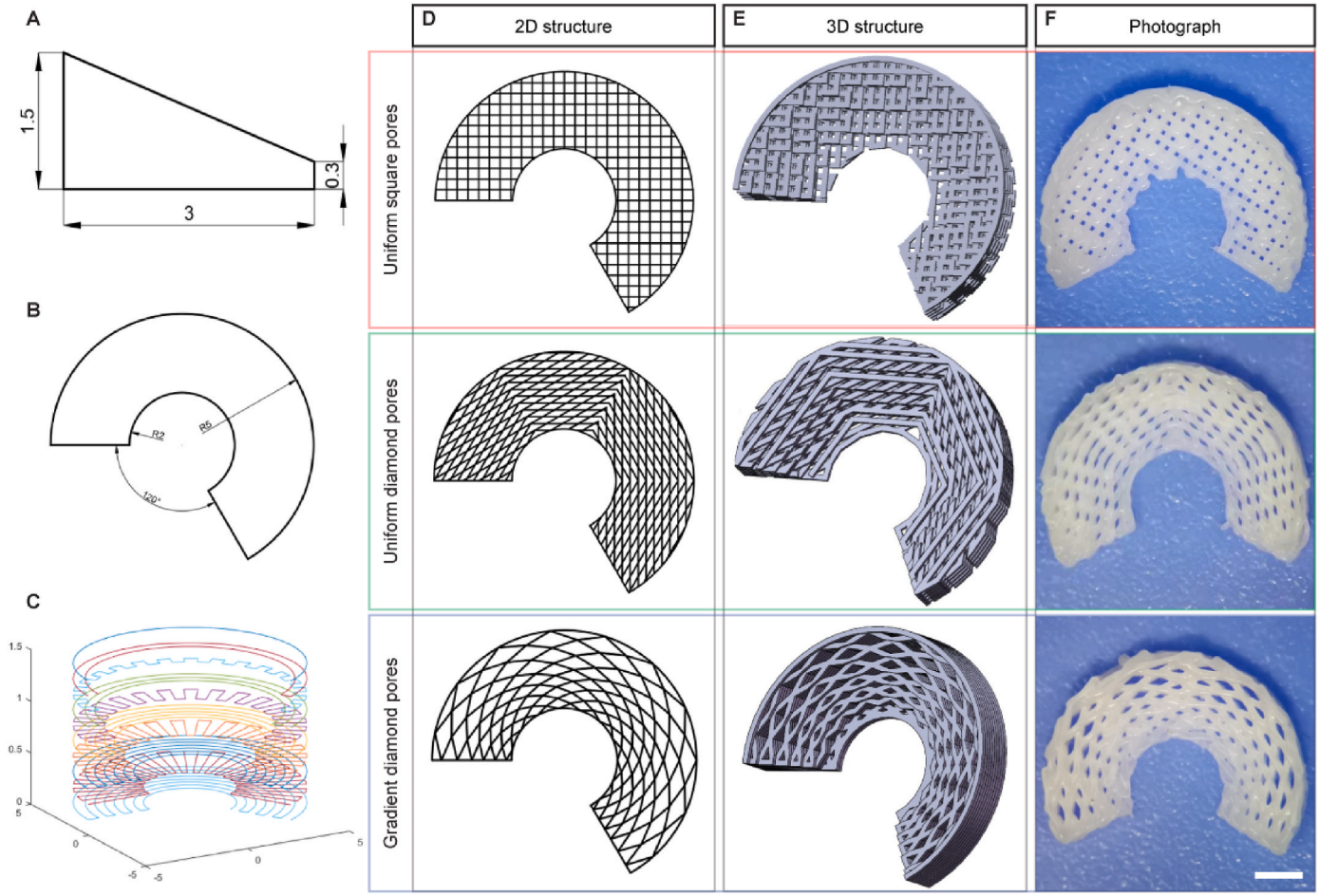

Fig. 2. Structural designs of the TEMs. A-C, Sectional view (**A**) and top view (**B**) of the PCL scaffolds. **C**, Path map of printing. **D-F**, 2D structural design (**D**), 3D structural design (**E**), and photographs (**F**) of the PCL scaffolds designed with uniform square pores, uniform diamond pores, and gradient diamond pores, respectively. Scale bar, 3 mm.

microstructures, including structure size, thickness, and space between two layers (Fig. 2).

2.2. Alkaline etching of the PCL scaffold

The 3D-printed PCL scaffolds with M_W: 150,000 were soaked in 70% (v/v) ethanol aqueous solution for 30 min after manufacturing. Then, the scaffolds were washed with distilled water 3 times, followed by soaking in 5 M NaOH solution for 2 h [20–22]. The scaffolds were ready for use after washing and drying thoroughly.

2.3. Evaluation of surface roughness using scanning electron microscope and confocal laser scanning microscopy

Samples of PCL materials and alkaline etched materials were prepared to evaluate the surface roughness. To be observed under scanning electron microscope (SEM), the samples were dehydrated with gradient graded ethanol (50%, 70%, and 90%) for 30 min and then surface metalized by sputter coating with gold. The morphology of the PCL scaffold and the cellular morphology of the adherent BMSCs were observed by JSM5600LV SEM (JEOL Ltd., USA). To be observed under confocal laser scanning microscopy, the samples were also completely dried using gradient concentration ethanol aqueous solution and then imaged by laser reflection of the sample surface and pseudocolor processing.

The water contact angle test was also employed to evaluated the PCL scaffolds with M_w: 150,000 before and after NaOH treatment, which were performed on the produced PCL film. The film were then treated with NaOH as introduced before. Contact angles of deionized water drops were recorded and calculated with *Image J* software.

2.4. Cell preparation

2.4.1. Cell isolation

BMSCs were isolated from New Zealand white rabbits. Approximately 2 mL of bone marrow was extracted from the rabbits' posterior superior iliac spine with a bone marrow puncture needle. The extraction was diluted at a ratio of 1:1 with phosphate buffered saline (PBS, Zhongshan Company, Beijing, China) and layered on top of Ficoll-Paque lymphocyte separation liquid (1.084 g/mL, GE Healthcare, USA). After centrifugation at 3000 rpm for 30 min at room temperature, the middle cell layer was collected, washed with PBS and centrifuged at 3000 rpm for 15 min. Subsequently, the precipitates were collected and suspended in the culture medium for further applications.

2.4.2. Cell culture

Cells were routinely cultured in 75 cm^2 cell culture dishes (Corning, USA) at 37 °C in a humidified atmosphere containing 5% (v/v) CO_2. α-MEM culture medium (Gibco BRL Co. Ltd., USA) supplemented with 10% (v/v) fetal bovine serum (FBS) (HyClone, USA), 100 U/mL penicillin, and 100 U/mL streptomycin (Huabei Pharmaceutical Factory, China) was used. Cells were grown to 80–90% confluence for 5 days, followed by detached with 0.25% (v/v) trypsin (Sigma Diagnostics, St. Louis, USA). Cell passaging was routinely performed every 2–3 days. Only passages 2 and 3 cells were used in this experiment.

2.4.3. Cell implantation on the PCL scaffold

The BMSCs were seeded onto PCL scaffolds at a density of $3x10^5$ cells per scaffold in 24-well plates. Cell-seeded PCL scaffolds were cultured in α-MEM medium supplemented with 10% (v/v) FBS, 100 U/mL penicillin, and 100 U/mL streptomycin for 1 week to permit cell attachment and colonization. Subsequently, CTGF (100 ng/ml; PeproTech, USA) and TGF-β3 (10 ng/ml; PeproTech, USA) were added into α-MEM. Fibrogenic inducible supplements [ascorbic acid (50 μg/ml)] and chondrogenic inducible supplements [0.1 μM dexamethasone, sodium pyruvate (100 μg/ml), l-ascorbic acid 2-phosphate (50 μg/ml), L-proline (40 μg/ml), and 1% 1xInsulin transferrin selenium (ITS)] were included in CTGF and TGF-β3, respectively, as we described before [13]. The medium was changed every 2 days. After culturing for different lengths, cell-loaded scaffolds were collected for various analyses (72 h for live/dead cell viability assay; 1, 7, 14 days for cell counting kit-8 (CCK-8) cytotoxicity evaluation and DNA content quantitation; 1 week for cellular morphology; 2 and 4 weeks for biochemical analysis).

2.5. Viability and proliferation of cells

2.5.1. Live/dead cell viability assay

The PCL scaffolds were seeded with BMSCs for 72 h before removal. After washing with PBS, the cell-loaded scaffolds were incubated for 2 h in live/dead staining buffer (Invitrogen, USA) consisting of calcein-AM (0.5 μL/mL) and propidium iodide (0.5 μL/mL) in PBS, as instructed by the manufacturer. The scaffolds were washed with PBS afterward and observed with a Leica TCS-SP8 confocal microscope (Leica, Germany). All fluorescent images were analysed by Image-Pro Plus software (v.6.0; Media Cybernetics). Quantitative data for cell viability were calculated according to live (green, wavelength 488 nm)/dead (red, wavelength 594 nm) staining by dividing the number of living cells (green) by the total number of cells.

2.5.2. Cytotoxicity evaluation

To evaluate the cytotoxicity of the scaffolds, the metabolic activity of cells was determined at various time points. On days 1, 7, and 14 of culturing BMSCs with the scaffolds in vitro, the cells were incubated with CCK-8 working solution (Invitrogen, USA) in the medium at 37 °C. After 2 h, the mean OD was measured at 450 nm using an ultraviolet spectrophotometer (Thermo Electron Corporation, USA).

2.5.3. DNA content quantitation

The biomass concentrations of the cell growth on scaffolds were determined by measuring the DNA contents at various time points. On days 1, 7, and 14 of culturing BMSCs with the scaffolds in vitro, the wet weights of the scaffolds were measured. Subsequently, the cell-loaded scaffolds were cultured in medium containing papain lysate (20 mg/mL, Sigma Diagnostics, USA) and Hoechst 33285 working solution (1 mg/mL, Sigma Diagnostics, USA) at 37 °C for 30 min. The OD value of the medium was measured using an ultraviolet spectrophotometer (excitation/emission = 360 nm/460 nm, Thermo Electron Corporation, USA). Calf thymus DNA (Sigma Diagnostics, USA) was used as the standard sample.

2.6. Differentiation of cells

2.6.1. Cellular morphology of BMSCs on the PCL scaffold

SEM and confocal microscopy were employed to observe high-resolution features of cells grown on the PCL scaffold.

After culturing in vitro for 1 week, the cell-seeded scaffolds were washed with PBS and fixed with 2.5% (w/v) glutaraldehyde (Zhongshan Company, China) for 2 h. After fixation, the scaffolds were each washed three times with PBS for 10 min and then dehydrated with gradient graded ethanol (50%, 70%, and 90%) for 30 min. Next, the scaffolds were completely dried using gradient concentration ethanol aqueous solution and then surface metalized by sputter coating with gold. The morphology of the PCL scaffold and the cellular morphology of the adherent BMSCs were observed by JSM5600LV SEM (JEOL Ltd., USA).

After culturing in vitro for 1 week, the cell-seeded scaffolds were washed with PBS, fixed with 4% (v/v) polymeric formaldehyde (Zhongshan Company, China) for 30 min at room temperature, and then permeabilized by incubating with 1% (v/v) Triton X-100 (Sigma–Aldrich, USA) for 30 min at room temperature. The scaffolds with fixed cells were treated with phalloidin (100.0 nM in PBS, Cytoskeleton Inc., USA) at 37 °C for 4 h and with Hoechst 33258 (1 mg/mL, Sigma Diagnostics, USA) at room temperature for 30 min. Next, the scaffolds

were washed with PBS for 15 min and then observed by a confocal laser scanning microscope (Leica TCS-SP8, Leica Microsystems, Germany). The cytoskeleton was stained red, and nuclei were stained blue.

2.6.2. Biochemical analysis

The glycosaminoglycans (GAG), type I collagen (COL-1), and type II collagen (COL-2) contents of the BMSCs on the PCL scaffold were quantified. After culturing BMSCs and the scaffolds in vitro for 2 and 4 weeks as described in 2.4, the cells on the scaffolds were treated in medium containing papain lysate (20 mg/mL, Sigma Diagnostics, USA) and 1,9-dimethylmethylene blue (DMMB, Sigma–Aldrich, USA) reagent at room temperature for 2 h. The GAG amounts were determined by measuring the OD spectrophotometrically using chondroitin sulfate as a standard [13,23]. The contents of COL-1 and COL-2 were determined using type I and II collagen ELISA kits (6016 and 6018, Chondrex Inc., USA), respectively, according to the manufacturer's instructions.

2.6.3. Immunofluorescence analysis

After culturing BMSCs and the scaffolds in vitro for 4 weeks, the medium was removed. The scaffolds were washed with PBS, fixed with 4% (v/v) polymeric formaldehyde (Zhongshan Company, China) for 30 min at room temperature, rinsed with PBS and sealed by incubation in PBST-BSA (1% BSA, 10% normal goat serum, 0.3 M glycine in 0.1% PBS-Tween, Thermo Corporation, USA) at 37 °C for 30 min. For detection of COL-1 and COL-2 by immunofluorescence, the scaffolds were incubated with the primary antibodies of goat anti-rabbit COL-1 antibody (ARG21965, Arigo, China; 8 μg/ml) and mouse anti-rabbit COL-2 antibody (CP18, Sigma–Aldrich, USA; 10 μg/ml) at 4 °C for 24 h, followed by incubation in donkey anti-goat IgG H&L (Alexa Fluor® 594) (ab150132, Abcam, USA) and Alexa Fluor® 488 goat anti-mouse IgG antibody (A28175, Thermo Fisher Scientific, USA) secondary antibodies at room temperature for 30 min. Scaffolds were washed with PBS and exposed to 0.1 mg/mL 4,6-diamidino-2-phenylindole (DAPI) (Sigma–Aldrich, USA) at room temperature for 15 min, followed by washing. The scaffolds were briefly air-dried and observed by a confocal laser scanning microscope (Leica TCS-SP8, Leica Microsystems, Germany).

2.6.4. Gene expression analysis

Real-time reverse transcription polymerase chain reaction (RT–PCR) was employed to assess gene expression. RNA was extracted using TRIzol (Thermo Corporation, USA) and reverse-transcribed using a reverse transcription kit (Promega Corporation, USA) after culturing for 2 and 4 weeks in vitro. The fibrochondrogenesis gene markers (*FN-1*, *TNC*), chondrogenesis gene markers (*ACAN*, *SOX-9*), and glyceraldehyde 3-phosphate dehydrogenase (*GAPDH*) were assessed using commercial primer sets (Invitrogen, USA). The related primer sequences are shown in the supplementary data. To normalize gene expression levels, *GAPDH* was employed as an internal control using the ΔΔCt method. RT-PCR was performed according to the presented sequences (Table S1).

2.7. Finite element analysis

A rectangle with a length of 10 mm and a width of 5 mm was drawn by ABAQUS (Dassault, SIMULIA, France), and the middle grid was filled with USSP, USDP and GSDP microstructures. The pore width is the same as the design of the 3D scaffold. The material was defined as an isotropic elastic material with a Young's modulus of 310 MPa and Poisson's ratio of 0.35. One end of the compression direction was completely fixed (each node limits all degrees of freedom), and the other end applied displacement constraints so that the displacement of the structure in the compression direction was 3% of the length of the direction. The displacement and force of each step are collected. The strain and stress were calculated according to the size of the structure and the compression direction, respectively, and then the Young's modulus was calculated according to the slope of the initial linear segment.

SolidWorks (Dassault systems S. A) software was used to design the dynamic compression finite element analysis model, including the lower meniscus scaffolds and the hemisphere used to simulate the mechanical environment of the knee joint, as we reported before. The diameter of the hemisphere is 10 mm. The height of the inner ring of the meniscus scaffold was 0.48 mm, the diameter of the inner ring was 4 mm, the height of the outer ring was 1.5 mm, and the diameter of the outer ring was 10 mm as we described before [13]. Save model as x_t. format and import it into ABAQUS for finite element analysis. The meniscus scaffold was set as an elastomer, with an elastic modulus of 30 MPa and Poisson's ratio of 0.35. The hemisphere was set as a rigid body. The lower bottom surface of the meniscus scaffold was fixed without deformation. When pressurized, the sphere pressed down 10% of the thickness of the meniscus scaffold.

2.8. Evaluation of mechanical properties of the scaffolds

In terms of the compression test, 3x3x3 mm cube were prepared as USSP, USDP and GSDP test pieces. The thickness and width of each test piece in three dimensions were measured and recorded. The pneumatic clamp of an Instron-5465 universal testing machine was used to tighten both ends of the test piece, the length of the test section was recorded (the length of the test section was approximately 5 mm), and then the compressive strength was tested at a rate of 0.005 mm/s until 90% of the original length of the test piece was reached. Then, the elastic modulus was calculated from the linear portion of the stress–strain curve.

In terms of the tensile test, 10x10x3 mm microstructures as USSP, USDP and GSDP test pieces were prepared. The thickness and width of each test piece were measured and recorded. The pneumatic clamp of an Instron-5465 universal testing machine (Zhujin Analytical Instrument Co., Ltd., Shanghai, China) was used to tighten both ends of the test piece, the length of the test section was recorded (the length of the test section was approximately 5 mm), and then the tensile strength in the radial and circumferential directions was tested at a rate of 0.5 mm/min until a nonlinear segment occurred (strain >5%). Then, the tensile modulus was calculated from the linear portion of the stress–strain curve. In terms of cyclic tensile and compressive test, standard test pieces were made as described above and 100 cycles were implemented as described before [24].

2.9. Surgical procedure

2.9.1. Knee joint implantation of scaffolds

The protocol was complied with the Guide for the Care and Use of Laboratory Animals published by the National Academy Press (National Institutes of Health Publication No. 85-23, revised 1996), and the procedures involving animal experiments were reviewed and approved by the IRB Medical Committee of Peking University Third Hospital (grant. A2022019). After culturing the cell-loaded scaffolds for 4 weeks in vitro, the scaffolds with different microstructure were implanted into rabbit knee. The rabbits were fixed on the operating table after anesthesia, and the knee joints were disinfected and covered with an operation sheet. The skin and subcutaneous tissue were cut along the inner zone of the patellar tendon, the medial retinaculum and some medial femoral muscles were cut off, the patella was dislocated, the knee joint was exposed, the anterior angle of the meniscus was cut off, the meniscus was separated to the posterior angle along the synovial edge, the anterior angle and body of the meniscus were clamped with curved pliers, and the posterior angle was completely removed. The medial collateral ligament was preserved to maintain the stability of the joint. In the transplantation group, TEM transplantation was performed as previously reported [25]. The whole meniscus was removed to construct a meniscectomy animal model. Then the scaffold was sutured to the adjacent synovium with non-resorbable No. 4-0 sutures (Ethicon, Somerville, NJ). The anterior and posterior horns of the implants were reconnected to the appropriate ligament structure. At the same time, attention was given to reduce side damage to the cartilage and joint

capsule during the operation. Finally, the joint capsule, subcutaneous tissue and skin were closed with No. 3-0 sutures (Ethicon, Somerville, NJ). The knee joint was not fixed after the operation, and the animals moved freely. A total of 400,000 units of penicillin were injected intramuscularly for 3 consecutive days. Six rabbits (bilateral) of each group were double-blinded collected at each timepoint for the biomechanical, histological and imaging evaluation.

2.9.2. In vivo degradation of PCL scaffolds

The study protocol was reviewed and approved by the Institutional Review Board of Peking University (PUIRB-LA2022629). The 3D-printed USSP, USDP, GSDP PCL scaffolds with M_w: 150,000 before and after NaOH treatment were sterilized with ethylene oxide. The scaffolds were weighted (W_0) and implanted into the subcutaneous tissue on the back of C57 mouse after anesthetization. The mice were sacrificed after 2, 4, 8 and 12 weeks by injection of a lethal dose of barbiturates. The covered connective tissue was removed and the scaffolds were thoroughly washed, dried and weighted (W_t). Then the in vivo degradation rate was calculated according the following formula as previously reported [22].

$$\text{Mass loss}\ (\%) = (W_0 - W_t) / W_0 \times 100\%$$

2.10. Evaluation of the neomeniscus

The rabbits were sacrificed 12 and 24 weeks after scaffold implantation. Magnetic resonance imaging (MRI) scans were employed to observe meniscus regeneration and arthritis in situ and were calculated by Whole-organ magnetic resonance imaging score (WORMS). Neomenisci were then grossly evaluated through the Gross Evaluation of Meniscus Implant Score [26]. After that, histological methods were employed to evaluate the cell phenotype and ECM distribution (COL-1, COL-2, GAG) of neomeniscus, including haematoxylin-eosin (H&E) staining, toluidine blue (TB) staining, immunohistochemical and immunofluorescence staining of COL-1 and COL-2, and the relative density descriptors of integral optical density (IOD)/area values were analysed to perform the semiquantification of COL-1 and COL-2 deposits through Image-Pro Plus software (v.6.0; Media Cybernetics). The neomeniscus were also cut into 2x5x10 mm specimens for the test of tensile modulus as described above.

2.11. Evaluation of cartilage

The surface cartilage degeneration of the knee joint was grossly evaluated according to the International Cartilage Repair Society (ICRS) cartilage injury classification system. Microcomputed tomography (micro-CT) was then employed to assess osteophyte formation and subchondral bone resorption in situ and bone volume fraction (BV/TV) & trabecular thickness (TB. Th) was calculated for quantitative analysis. After that, histological methods were employed to evaluate the cell phenotype and GAG distribution of articular cartilage, including H&E staining, TB staining and Safranin O and Fast Green (SO&FG) staining, and the Mankin score was calculated for quantitative analysis.

2.12. RNA-seq experiments

The scaffold was cut into two parts with a pore size of 215 μm as the boundary and the total RNA of cells was extracted from the inner and outer zones of GSDP-TEM with TRIzol (Invitrogen, USA) reagent, and the genomic DNA was removed with DNase I (Takara). Then, the RNA quality was determined by a 2100 Bioanalyzer (Agilent, USA) and quantified by ND-2000 (Nanodrop Technologies, USA). For high-quality RNA samples after quantitative detection (OD260/280 = 1.8–2.2, OD260/230 ≥ 2.0, RIN≥ 6.5, 28S:18S ≥ 1.0, >1 μg). The RNA-seq transcriptome library was prepared following the TruSeq™ RNA Sample Preparation Kit from Illumina (USA) using 1 μg of total RNA. Then, according to the PolyA selection method, messenger RNA was isolated by oligomer (DT) beads and fragmented by fragment buffer, and double-stranded cDNA was synthesized by a Superscript Double-Stranded cDNA Synthesis Kit (Invitrogen, USA) and random hexamer primers (Illumina, USA). Then, according to Illumina's library construction scheme, the synthesized cDNA was subjected to terminal repair, phosphorylation and "A" base addition. The library of cDNA target fragments with a size of 300 bp was selected on 2% Low Range Ultra Agarose, and then PCR amplification of 15 PCR cycles was carried out by Phusion DNA polymerase (New England Biolabs, Inc., UAS). After quantification by TBS380, the paired terminal RNA SEQ sequencing library was sequenced using an Illumina NovaSeq 6000 sequencer. After data quality control and comparison with the reference genome, differential expression analysis and functional enrichment of differentially expressed genes were performed. To determine the differentially expressed genes (DEGs) between two different samples, the expression level of each transcript was calculated according to the transcripts per million reads (TPM) method. RSEM was used to quantify gene abundance. The DEGs with log2FC > 1 and Q value < 0.05 (DESeq) were statistically significant. In addition, GO and KEGG functional enrichment analyses were carried out to determine the functional enrichment field of DEGs of BMSCs inside and outside the scaffold and the related gene pathways leading to the spatially specific heterogeneous differentiation of BMSCs inside and outside the scaffold.

2.13. Statistical analysis

All statistical analyses were performed using SPSS (v.23.0, IBM, USA).

3. Results

3.1. GSDP-TEM shows biomimetic mechanical heterogeneity similar to that of the natural meniscus

To evaluate the potential of the GSDP-TEM in restoring natural meniscus biomechanical functions, its 2D and 3D dynamic compression responses were investigated using finite element analysis (FEA) and compared to those of the uniformly structured TEMs (Fig. 3A–B). The GSDP-TEM demonstrated the greatest biomimetic and heterogeneous stress distribution ability in both 2D and 3D FEA. The 2D compression response was simulated by applying compression loads from two perpendicular directions onto mesh structures with different pore designs (Figure S2A). The proposed gradient design of the GSDP-TEM showed direction-related heterogeneous stress distributions (Fig. 3A) with a significant difference in the instantaneous Young's modulus of 1.85 MPa radially against 29.86 MPa in the circumferential direction (Fig. 3E, C). The 3D dynamic compression response was modelled to mimic the mechanical environment in the knee joint under natural body weight (Figure S2B). The meniscal-shaped PCL models with no porous structure presented solely compressive stress and no tensile stress under compression (Figure S2C). The TEMs with diamond pores exhibited tensile strains on the outer zone and compressive strains on the inner zone, consistent with the natural meniscus (Fig. 3B). However, unlike the natural meniscus [27], the stress distribution of the USDP-TEM was exceptionally irregular over the entire structure, with high tensile stress presented not only on the outer edge but also in the middle of the scaffold (Fig. 3B–Movie. S1). Thus, the USDP-TEM could not transmit the axial load into tensile stress adequately, impeding its chondroprotection ability. In contrast, the proposed gradient topology presented evenly distributed compressive stress on the inner zone, which gradually transitioned into tensile stress on the outer side (Fig. 3B–Movie. S2). Such a stress distribution of the GSDP-TEM in response to the vertical compression load was remarkably similar to that of the natural meniscus under body weight [28].

Crescent-shaped wedge-like TEMs with different microstructures

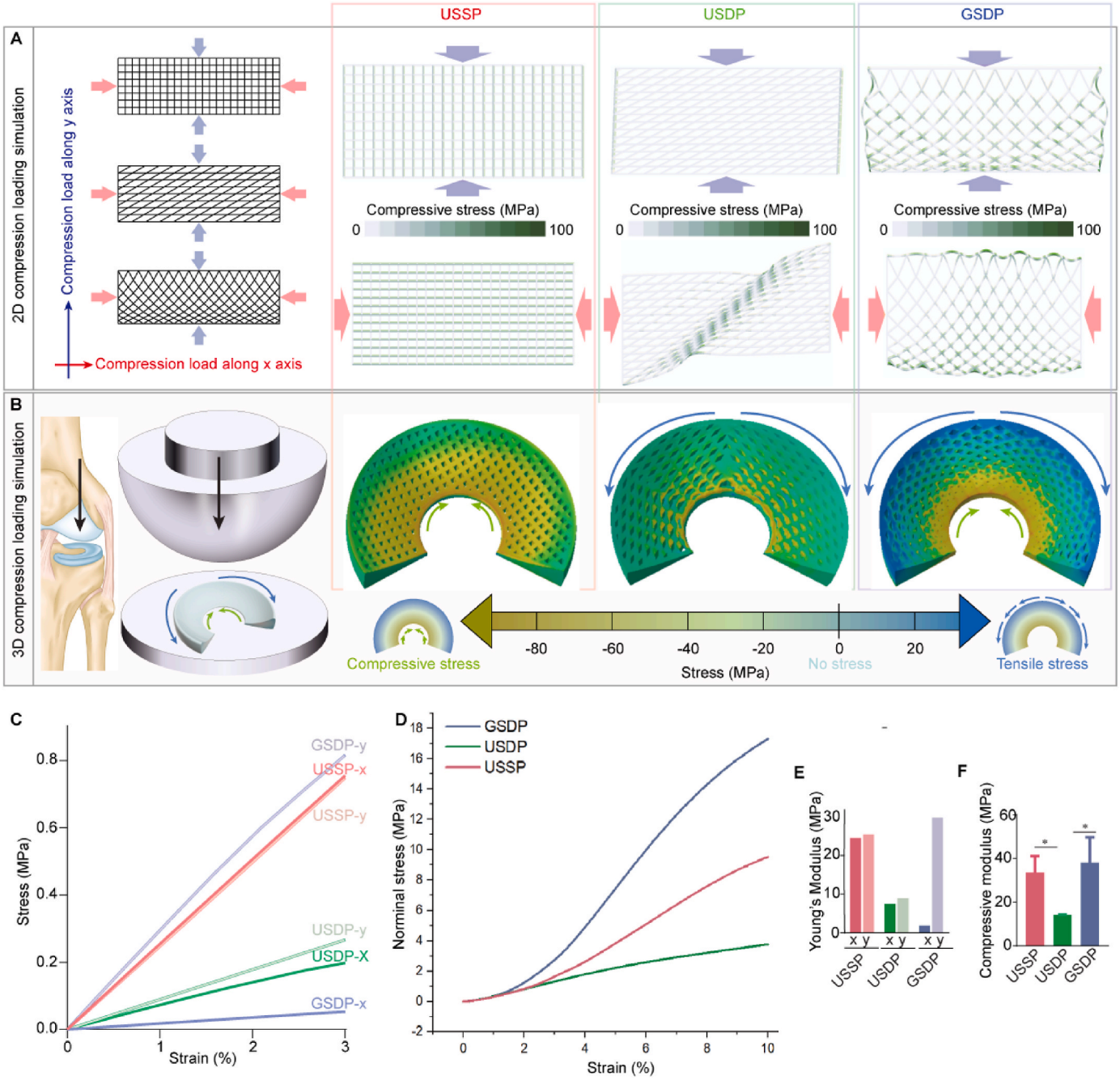

Fig. 3. GSDP-TEM exhibits gradient heterogeneous mechanical behaviors mimicking the natural meniscus. A, 2D dynamic compression FEA of uniform and gradient structures. Gradient structure showed heterogeneous stress distribution when the compression loads were applied in the circumferential (x) and radial (y) directions. **B**, 3D dynamic compression finite element analysis of USDP-TEM and GSDP-TEM. The GSDP-TEM exhibited best biomimetic load transmission properties. **C**, E Stress-strain curves (C) and the corresponding instantaneous Young's modulus (E) of the 2D dynamic compression FEA on USDP-TEM and GSDP-TEM. **D, F**, The stress-strain curves (D) and corresponding calculated compressive modulus (**F**) of USDP-TEM and GSDP-TEM. The statistical analysis in **F** were performed using One-way ANOVA with Tukey's post-hoc test. *P $<$ 0.05. Data are shown as mean $\pm$ s.e.m.

were 3D-printed and standard test piece (3x3x3 mm cube) were constructed for compression (Figure S2D) and tensile tests (Figure S2E) to further evaluate their mechanical performances. The schematic illustrating load directions upon testing TEMs with different design parameters was showed in Figure S2F. In order to detect the tensile and compressive modulus of scaffolds, unidirectional tensile/compressive experiments were conducted until the scaffolds collapsed. In addition, the tensile tests were employed both in radial and circumferential direction. The tensile/compressive modulus was then calculated according to the stress-displacement curve. The GSDP-TEM and USDP-TEM showed heterogeneous tensile modulus radially and circumferentially under tensile strain (Figure S2G-H). GSDP-TEM showed higher circumferential tensile modulus, which exhibits high similarity to those of the natural meniscus, while the USSP-TEM failed to achieve such biomechanical properties (Figure S2G-H). The compression modulus of the proposed GSDP-TEM was significantly higher than that of the USDP-TEM, which indicated a stronger ability to resist compressive pressure (Fig. 3D, F). In addition, cyclic tensile and compressive tests were conducted to the assess the performance of the PCL scaffolds and the results are shown in Figure S3. After the second cycle of consecutive cyclic

tensile and compressive tests, the overlap of the loading-unloading curves proved the excellent elasticity and durability of PCL scaffolds. Overall, the mechanical simulation and testing results illustrated that the gradient design of the GSDP-TEM with broad similarities to the heterogeneous mechanical behaviors of the natural meniscus outperformed the uniform TEMs as a meniscal replacement.

3.2. Molecular etching balances the mechanical properties and biocompatibility of high M_w PCL scaffolds

To increase the roughness and hydrophilicity of the material surface, 3D-printed poly(ε-caprolactone) (PCL) scaffolds were treated with alcohol and NaOH solution. The surface roughness analysis showed that the overall height decreased after alkaline treatment, with ravines and gullies crisscrossing the surface (Fig. 4A). The water contact angle results of PCL films (M_w: 150,000) with treatment of 5 M NaOH are shown in Figure S4. The water contact angles of PCL films before and after treatment were 80.34° ± 3.28° and 50.73° ± 5.08°, respectively, indicating that the hydrophilicity of the PCL surface increased after treated with 5 M NaOH.

The rougher PCL strand surfaces were more beneficial to BMSCs attachment, viability, and proliferation (Fig. 4B). The tensile strength was only reduced by approximately 6.6% (Fig. 4B). Therefore, 3D printing using high- M_w PCL followed by alkaline etching was employed to manufacture a scaffold with optimized mechanical strength and biocompatibility.

The in vivo mass loss of NaOH treated GSDP-TEM, USDP-TEM and USSP-TEM after 12 weeks are 36.57 ± 2.21%, 29.63 ± 5.64% and 25.87 ± 3.5%. The in vivo mass loss of un-treated GSDP-TEM, USDP-TEM and USSP-TEM after 12 weeks is 26.17 ± 1.2%, 23.4 ± 0.7% and 22.3 ± 2.71%. Significant difference was found between the treated and untreated groups of GSDP and USDP-TEM, indicating that NaOH etching can accelerate the degradation rate of PCL scaffolds (Figure S5).

3.3. Diamond micropores induce superior BMSCs proliferation

The viabilities of seeded BMSCs on the inner and outer zones of the TEMs with different design parameters (USSP, USDP, GSDP) were compared to evaluate the structural designs. The live/dead staining assay results illustrated that BMSCs grown on the TEMs with diamond-shaped pores presented higher overall viability compared to those grown on the TEMs with square-shaped pores (Fig. 4C, Figure S6). The CCK-8 cytotoxicity assay (Fig. 4D) and DNA content results (Fig. 4E) indicated a continuous increase in the cells' metabolic activity during the culturing of cells and TEMs for 14 days. The BMSCs presented a better proliferative effect on the TEMs with diamond-shaped pores (uniform or gradient) than on those with square-shaped pores. Thus, the diamond micropore, more suitable for promoting cell proliferation than the square micropore, was selected for the structural design of the TEM in the present study.

3.4. Gradient diamond micro-structure induces heterogeneous cell differentiation

The BMSCs on the GSDP-TEM in the inner zone appeared more rounded in shape (Fig. 5A, B) and secreted more COL-2 (Fig. 5F, G) and GAG (Fig. 5H), while the cells in the outer zone appeared more oval, were fusiform-like in phenotype (Fig. 5A, C) and secreted more COL-1 (Fig. 5D, E). The quantitative evaluation of the COL-1, COL-2, and GAG contents after in vitro culture for 4 weeks confirmed that the BMSCs grown on the outer region of the GSDP-TEM secreted a significantly higher level of COL-1 (Fig. 5H), and those grown on the inner zone of the GSDP-TEM secreted significantly more COL-2and GAG (Fig. 5H). The ECM deposition after 2 weeks was also detected and no significant difference was found regarding the level of COL-1 on the different zone of GSDP-TEM, while COL-2 deposition was significantly higher in the inner zone than that of outer zone (Figure S7 left). In comparison, the uniform TEMs were proven in the present study to be unable to contribute to regional-specific BMSCs differentiation, with no visual difference presented in the morphologies and ECM depositions of the BMSCs grown on the inner and outer zones of the TEMs (Figure S8). The fibrogenic and chondrogenic gene expression for 2 weeks (Fig. 5J) and 4 weeks (Figure S7 right) culture were also consistent with the heterogeneous cell phenotypes on the GSDP-TEM, while no regional-specific significant differences were observed for the USDP-TEM. BMSCs were distributed both on the surface of PCL fibres and the middle of pores (Figure S9), but the latter was inevitably removed due to the experimental operation. The results showed that the GSDP-TEM successfully induced heterogeneous BMSC differentiation and ECM construction with position-dependent contents in vitro.

3.5. GSDP-TEM induces heterogeneous meniscus regeneration in vivo

To evaluate the in vivo performance of the proposed GSDP-TEM for meniscal regeneration, implantation was performed on rabbits after total medial meniscectomy, as illustrated in Figure S10. The appearance of meniscal-like tissue (neomeniscus) was observed at 12 weeks after GSDP-TEM implantation. Macroscopically, all groups, regardless of the implanted scaffold structure, regenerated a piece of soft tissue (Figure S11). Notably, the meniscus regenerated after GSDP-TEM implantation was more biomimetic of the native meniscus in terms of macroscopic appearance than that regenerated after USDP-TEM implantation. The gross score of the neomeniscus [29] of the GSDP-TEM was significantly higher than that of the uniformly structured TEMs, indicating that the shape, position, and size of the neomeniscus in the GSDP-TEM implantation group was more biomimetic than that in the USDP-TEM group (Fig. 6B).

According to histological analysis, the neomeniscus regenerated with the GSDP-TEM exhibited the cell phenotype and ECM composition distribution similar to those of the natural meniscus. The cells on the scaffold appeared more round in shape towards the inside, while the cells appeared oval and fusiform-like in shape towards the outside, as illustrated via H&E staining (Fig. 6E). COL-1, COL-2 and GAG deposition was also examined by immunofluorescence (Fig. 6A), immunohistochemistry and TB staining (Fig. 6E) respectively. IOD/area of COL-2 was calculated to semi-quantify the expression level (Fig. 6D). The results showed that well-aligned fibrous tissue (with abundant COL-1 deposition) was distributed in the outer zone of the neomeniscus, while cartilage-like matrix (with abundant COL-2 and GAG deposition) was gradually distributed in the inner zone. The results were consistent with the in vitro validation and indicated that neomeniscus regenerated from the GSDP-TEM possessed biochemical heterogeneity, similar to the natural meniscus. No severe inflammatory cell infiltration was found in three groups according to the histological evaluation of synovium (Figure S12).

MRI scanning was employed to illustrate the neomeniscal condition in the rabbit knee in situ (Fig. 6F). Distinct signals in the meniscal triangle region of the coronal and sagittal planes were observed for the group implanted with the GSDP-TEM, indicating the regeneration of meniscal-like tissue. The knee MRI score [30] was calculated based on the MRI images to analyse the overall health status of the knee joint. The high score of the gradient scaffold group indicated that the GSDP-TEM has better effects on meniscal regeneration than the uniformly structured TEMs (Fig. 6C).

The biomechanical property of scaffolds after implantation for 24 weeks were tested. The tensile modulus of neomenisci of USDP (87.77 ± 5.57 MPa) and GSDP (92.1 ± 6.85 MPa) groups was significantly higher than that of USSP group (50.07 ± 4.61 MPa). No significant difference was found between the USSP and GSDP group, but both of them showed similar tensile modulus to the natural meniscus (Figure S13).

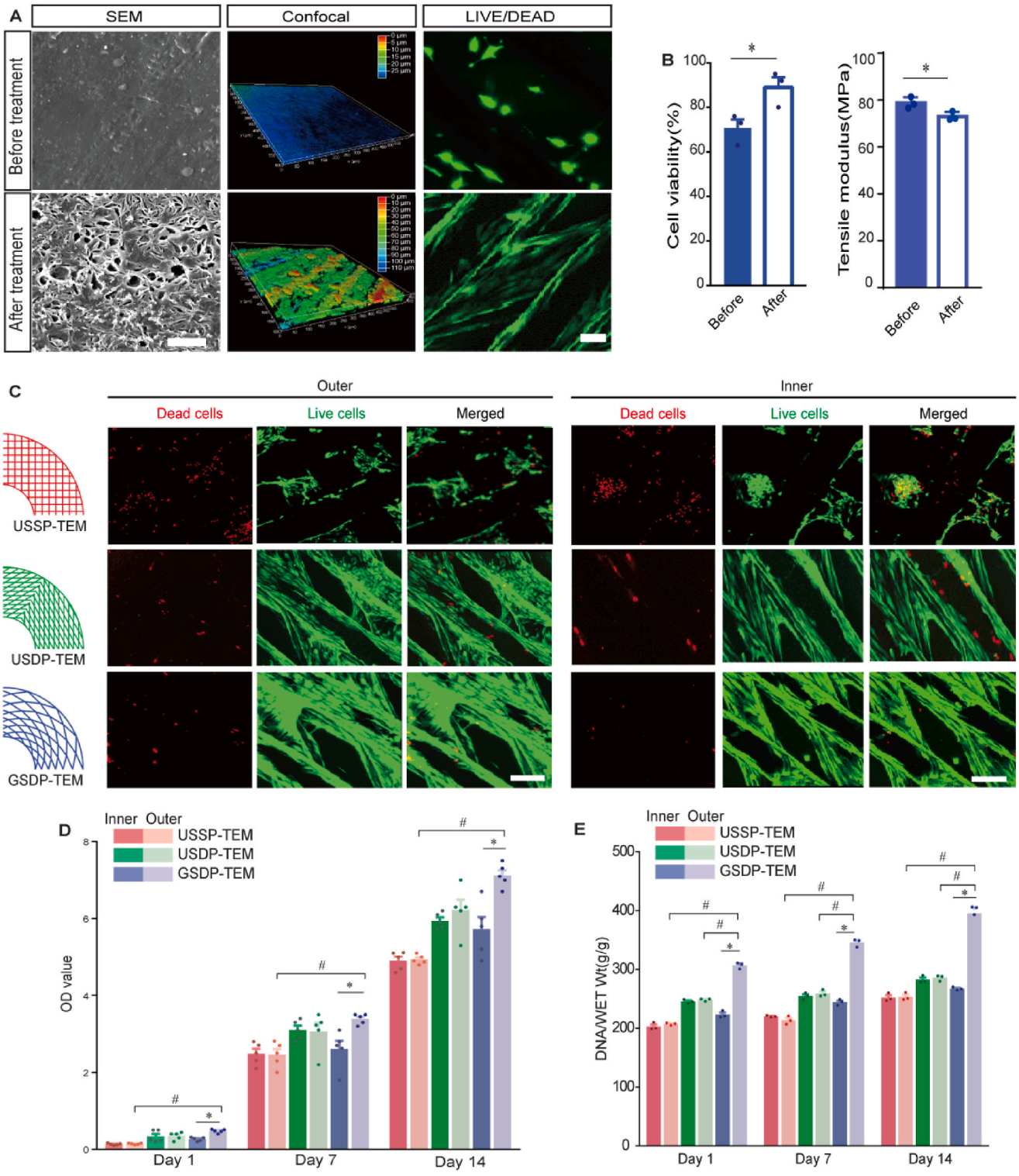

Fig. 4. Molecular etching and the diamond pores benefit BMSCs viability and proliferation. A, SEM images (scale bar, 10 μm), confocal microscopy detection reconstructions, and LIVE/DEAD staining results (scale bar, 200 μm) of M_w: 150000 PCL scaffold before and after NaOH etching were presented. The surface roughness and cell compatibility of scaffolds increased after NaOH etching. **B**, Left: Pooled data of cytocompatibilities of PCL scaffolds with different molecular weights, and before/after NaOH etching. The cell viability increased after treatment (n = 3 per group). Right: Tensile modulus of PCL scaffolds before/after NaOH etching (n = 3 per group). The statistical analysis was performed using two-tailed t tests: *P < 0.05. Data are shown as mean ± s.e.m. **C**, Representative fluorescence micrographs showing live (calcein-AM, green) and dead (propidium iodide, red) staining of BMSCs cultured for 3 days on the inner and outer side of USSP-TEM, USDP-TEM, and GSDP-TEM. Scale bars, 200 μm. **D-E**, Pooled data of the CCK-8 test (n = 5 per group) (**D**) and DNA content (n = 3 per group) (**E**) of the cells on the USSP-TEM, USDP-TEM, and GSDP-TEM. The statistical analysis in D and E were performed using One-way ANOVA with Tukey's post-hoc test. *P < 0.05, significant difference was found between inner and outer part of GSDP-TEM; #P < 0.05, significant difference was found between the outer part of USSP-TEM and GSDP-TEM, or the outer part of USDP-TEM and GSDP-TEM. Data are shown as mean ± s.e.m.

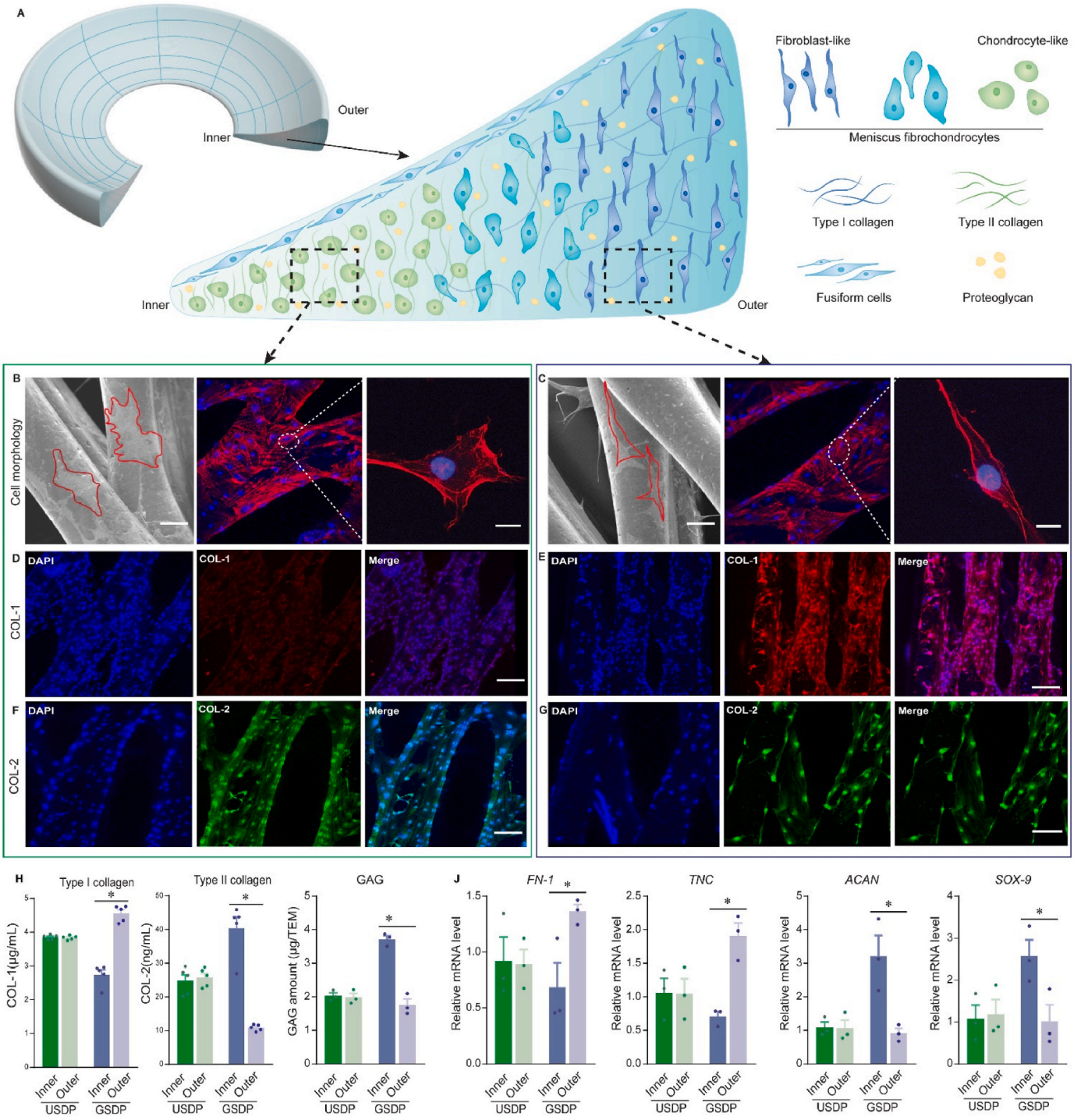

Fig. 5. The gradient variated pore sizes induce biomimetic heterogeneous cell differentiation. **A**, Schematic of heterogeneous structure of the natural meniscus. **B–C**, SEM and cytoskeleton detection of the inner and outer zones of GSDP-TEM. The morphology of the cells on the inner zone (**B**) of GSDP-TEM tended to be oval, while the cells on the outer zone (**C**) of the scaffold tended to be spindle. **D-E**, Detection of COL-1 content on the inner and outer zones of GSDP-TEM. BMSCs on the outer zone (**D**) of the GSDP-TEM secreted more COL-1 (red) than the inner zone (**E**). **F-G**, Detection of COL-2 deposition on the inner and outer zones of GSDP-TEM. BMSCs on the inner zone of GSDP-TEM (**F**) secreted more COL-2 (green) than the outer zone (**G**). Scale bars in **B-G**, 50 μm. **H**, Quantitative examination of COL-1 and COL-2 content on the inner and outer zones of USDP and GSDP-TEMs, respectively (n = 5 per group). **J**, Quantitative analysis of GAG content in the ECMs of BMSCs on the inner and outer side of the USDP and GSDP-TEMs, respectively (n = 3 per group). BMSCs were co-cultured with the scaffolds in vitro for 2 weeks. mRNA expression levels of fibrogenesis genes (*FN-1*, *TNC*) and chondrogenesis genes (*ACAN*, *SOX-9*) of BMSCs grown on the inner and outer sides of the USDP and GSDP-TEMs, respectively (n = 3 per group). The statistical analysis in **H** and **J** were performed using two-tailed t tests: *P < 0.05. Data are shown as mean ± s.e.m.

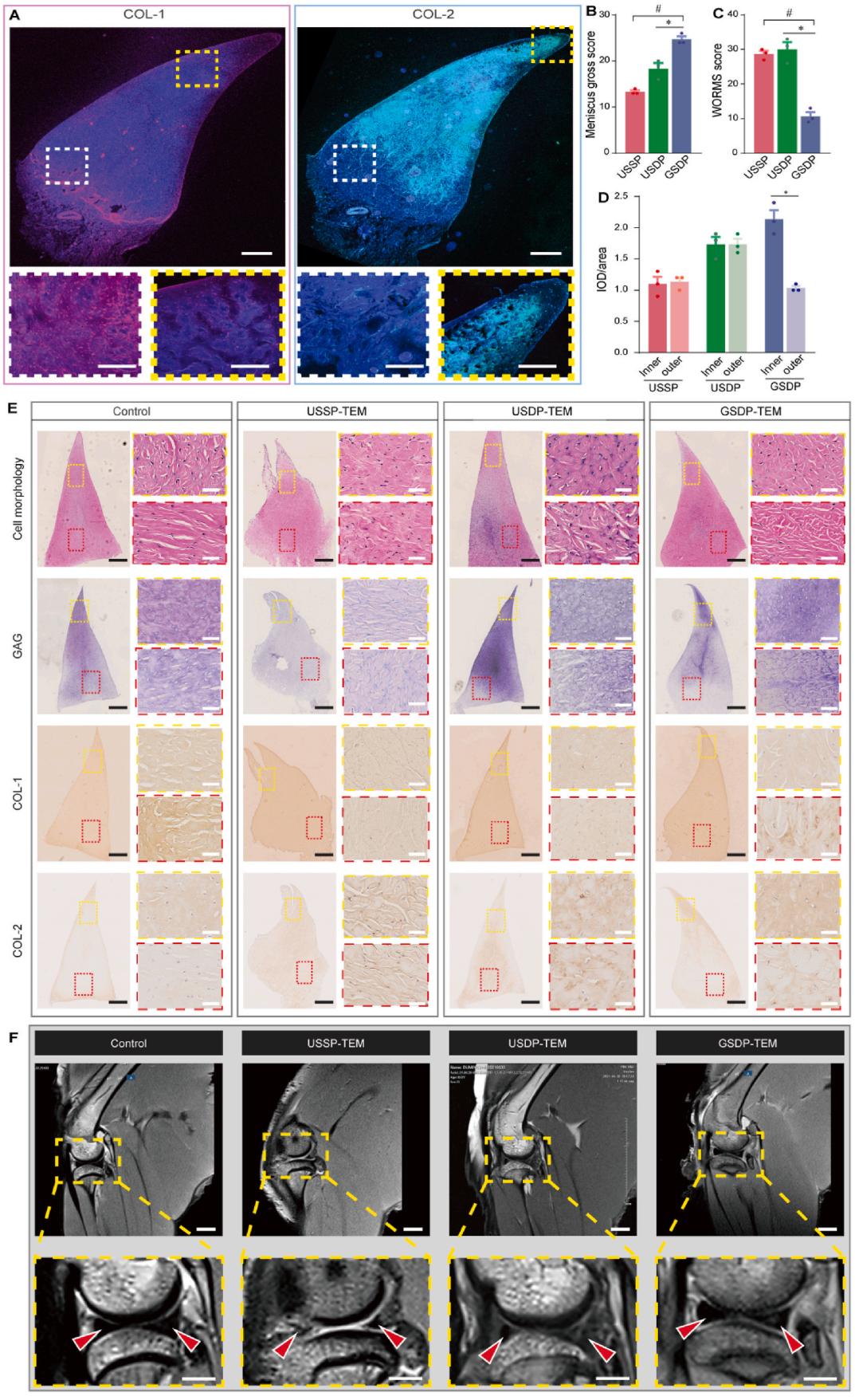

(caption on next page)

Fig. 6. GSDP-TEM induces in vivo regeneration of neomeniscus with high similarity to the natural meniscus. A, Immunofluorescence analysis of COL-1 and COL-2 distribution in neomenisci 24 weeks after GSDP-TEM implantation. **B-D**, Meniscus gross score (**B**), WORMS (**C**), and integral optical density (IOD)/area of COL-2 (**D**) of the neomeniscus regenerated from USSP-TEM, USDP-TEM and GSDP-TEM. The statistical analysis in **B** and **C** were performed using One-way ANOVA with Tukey's post-hoc test. *P < 0.05, significant difference was found between USDP and GSDP; #P < 0.05, significant difference was found between USSP and GSDP; The statistical analysis in **D** was performed using two-tailed *t*-test: *P < 0.05. Data are shown as mean ± s.e.m. n = 3 per group. **E,** Histology analysis of regenerated menisci after 24 weeks implantation in vivo. Cell morphologies were examined by H&E staining (Row 1). The glycosaminoglycans (examined using TB staining) (Row 2), COL-1 (Row 3), and COL-2 (Row 4) contents in the ECM were also examined by immunohistochemistry. Black scale bars, 400 μm, white scale bars, 100 μm. **F,** MRI of regenerated menisci after 24 weeks implantation in vivo. Sagittal position of MRI of knee joint 24 weeks without (control) or with implantation of USSP-TEM, USDP-TEM and GSDP-TEM. The regenerated menisci were presented with low-signal images between the tibial plateau and femoral condyle. Scale bars, 50 μm.

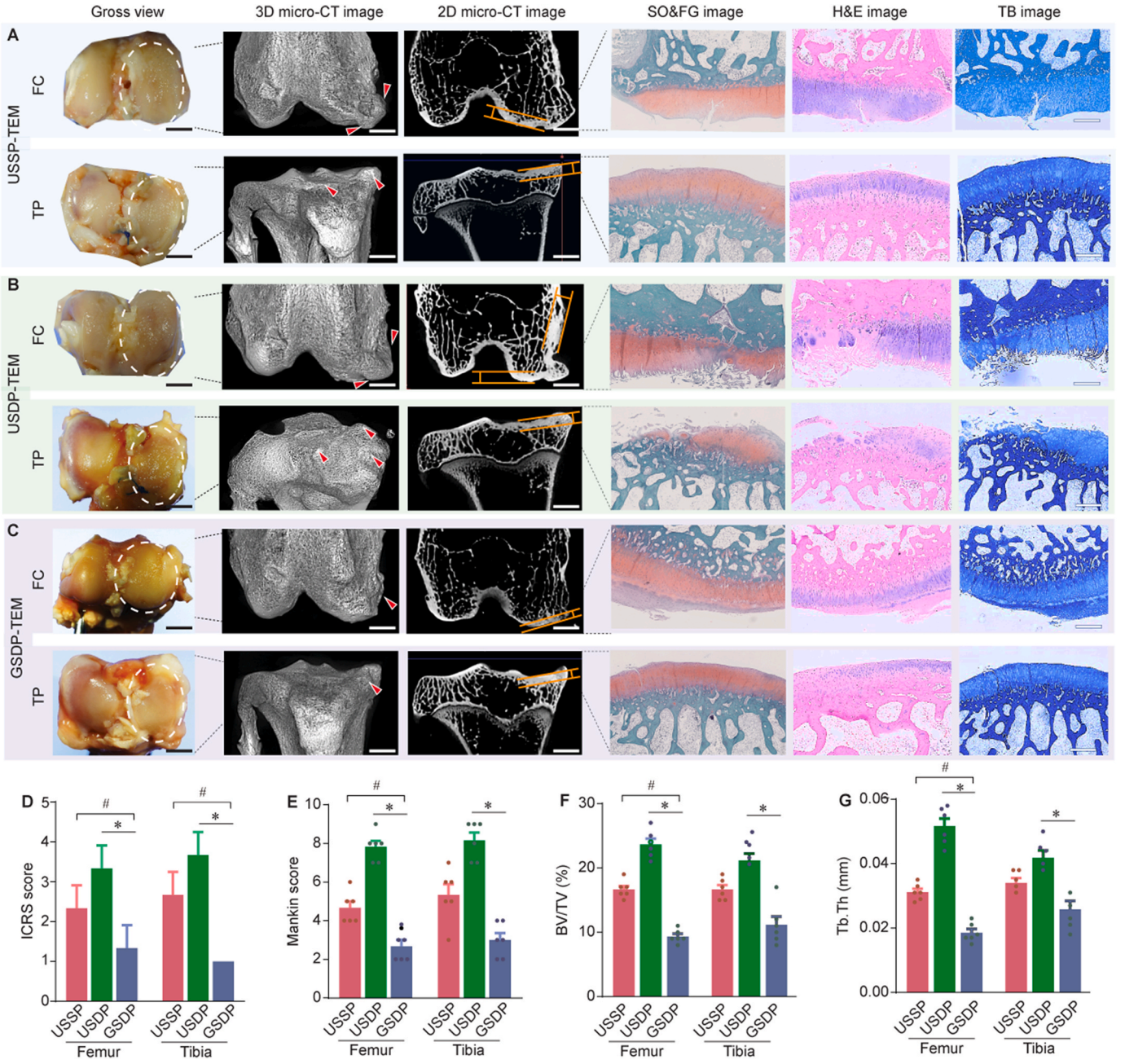

Fig. 7. GSDP-TEM restored the chondral protection function of the natural meniscus in vivo. A-C, Gross evaluation, 3D and 2D micro-CT images, and histological staining images (SO&FG, H&E, TB) of the femoral condyle and tibial plateau 24 weeks after implantation of USSP-TEM (**A**), USDP-TEM (**B**) and GSDP-TEM (**C**). Red arrows in 3D micro-CT images indicate osteophytes. **D-G**, Pooled data of ICRS score (**D**), Mankin score (**E**), BV/TV (**F**) and Tb.Th (**G**) of the tibial plateau and femoral condyle after implantation with USDP-TEM and GSDP-TEM. FC and TP represent femoral condyle and tibial plateau, respectively. The statistical analysis were performed using One-way ANOVA with Tukey's post-hoc test. *P < 0.05, significant difference was found between USDP and GSDP; #P < 0.05, significant difference was found between USSP and GSDP. Data are shown as mean ± s.e.m. Scale bars, 500 μm.

3.6. GSDP-TEM shows chondroprotective biofunction and alleviates joint degeneration in vivo

Joint cartilage from the rabbit knees after scaffold implantation was collected to assess OA progression to evaluate the restoration of natural meniscus biofunctions by the GSDP-TEM. Macroscopic observations (Fig. 7A–C) and the ICRS cartilage injury classification system [31] (Fig. 7D)were employed to visually evaluate the ability of the neomeniscus to protect articular cartilage. The articular cartilage surface of the GSDP-TEM group was smooth with barely visible degeneration, while the groups implanted with uniform TEMs showed more severe articular cartilage degeneration. According to a previous study, the chondroprotection ability of the meniscus is associated with its load transmission and absorption capacity [32]. Consequently, histological analysis was applied to quantitively evaluate the cartilage protection ability of the GSDP-TEM (Fig. 7A–C). The cartilage surfaces of the GSDP-TEM implantation group were observed to have complete anatomical structures, no apparent abnormalities in staining, uniform cell distributions, and high similarities to normal cartilage. In comparison, discontinuous defects, stratification, and shallow cracks of cartilage were observed in the uniformly structured TEM groups. The Mankin score was calculated based on the histological observation, and the GSDP-TEM group had a significantly lower Mankin score than the uniformly structured TEM groups (Fig. 7E).

The damage level variance was also evaluated by micro-CT examinations (Fig. 7A–C). In this regard, 3D reconstructed micro-CT images were obtained to analyse the bone phenotype of the rabbit knee joints without meniscus replacement (control) and with replacements of different TEMs. The knee joints with GSDP-TEM implantation presented significantly minimal osteophyte formation (highlighted with red arrows) and subchondral bone remodelling in both the fibular condyle and tibial plateau compared to those with USDP-TEM implantation (Fig. 7A–C). The results implied that the minimum OA level was achieved by the GSDP-TEM, not the USDP-TEM. BV/TV and Tb.Th. were evaluated based on the micro-CT images, and increases in these values indicated OA development on both the fibular condyle and tibial plateau [33]. The knee joints that underwent meniscus replacement appeared to have a higher BV/TV and Tb.Th. In particular, the group with GSDP-TEM implantation presented lower BV/TV and Tb.Th. (Fig. 7F–G), illustrating that OA was remarkably alleviated in this group compared to the groups with uniformly structured TEMs implantation.

3.7. Molecular mechanism for GSDP-TEM-induced biological heterogeneity construction

Eukaryotic transcriptome sequencing was employed to explore the underlying molecular mechanism of the biological heterogeneity induced by the GSDP-TEM. BMSCs seeded in the inner and outer zones of the GSDP-TEM were isolated for RNA sequencing after 2 weeks of culturing in vitro. Principal component analysis (PCA) of gene expression profiling showed significant separations between clusters of two groups, indicating significant differences in gene expression (Fig. 8A, Figure S14A). The inner 3 and outer 3 were excluded according to the PCA results. DEGs in the sequencing of cells in the inner and outer zones of the GSDP-TEM were analysed through a volcano map and a heatmap (Fig. 8B–C). A total of 637 upregulated genes on the outer side of the GSDP-TEM and 1058 upregulated genes in the inner zone of the GSDP-TEM were detected (Figure S14B), indicating that BMSCs under the influence of scaffold topology and growth factors showed regional-specific differentiation on the GSDP-TEM.

After the broad-spectrum RNA sequencing of the gene expression profiles, gene ontology (GO) and Kyoto Encyclopedia of Genes and Genomes (KEGG) pathway enrichment analyses were applied to analyse the biological functions of the DEGs. All the GO terms were divided into three domains: biological processes, cellular components, and molecular functions (Fig. 8D). To elaborate, GO enrichment analysis revealed that the DEGs in the biological process category were mainly involved in cellular processes, metabolic processes, and biological regulation, which were related to heterogeneous BMSCs differentiation. It also revealed that cell parts and membranes were enriched in cellular components, indicating that the scaffold microstructure and growth factors affected the deposition of ECM components, such as COL-1 in the outer zone and COL-2 in the inner zone of the GSDP-TEM.

In addition, KEGG pathway enrichment analysis was applied to identify crucial pathways for the regional-specific differentiation of BMSCs on the GSDP-TEM. *PDGFRA*, *LPAR2*, *SYK*, *TGFA*, *FGF7* were upregulated in the outer zone of GSDP-TEM, which are related with the fibrogenesis process and COL-1 generation [34–38]. Those DEGs were also enriched in the PI3K-Akt signalling pathway according to the KEGG analysis (Fig. 8E). Moreover, *SERPIN E1*, *BMP-6*, *BMPR* were upregulated in the inner zone of GSDP-TEM, which are related with the chondrogenesis process and COL-2 generation [39–41]. Those DEGs were also enriched in the P53 and TGF-β signalling pathway according to the KEGG analysis (Fig. 8E). Therefore, based on KEGG enrichment analysis, we hypothesized that the PI3K-Akt signalling pathway, P53 and TGF-β pathway may played essential roles in the regional-specific BMSCs differentiation induced by the microtopology effect of GSDP-TEM. Subsequently, gene set enrichment analysis (GSEA) was applied to confirm the expression of genes related to the PI3K-Akt and the P53 signalling pathway (Fig. 8F). Overall, we tentatively speculated that under the influence of the GSDP-TEM microtopology and growth factors, the P53 pathway and the PI3K-Akt pathway were activated, leading to biological heterogeneity construction. Therefore, based on preliminary analysis, we hypothesized that the PI3K-Akt signalling pathway, P53 and TGF-β pathway may played essential roles in the regional-specific BMSCs differentiation induced by the microtopology effect of GSDP-TEM. In-depth research will be conducted to confirm this discovery.

4. Discussion

Functional meniscus reconstruction with biological and biomechanical heterogeneities was the greatest challenge for TEM. The present study introduced the microtopology-induced effect on biological and biomechanical adjustment through the GSDP-TEM with gradient diamond-pored structures. Biologically, the GSDP-TEM microtopology mediated regional-specific BMSCs differentiation, achieving gradient biological heterogeneity self-construction. Biomechanically, the GSDP-TEM possessed excellent circumferential tensile modulus, load transfer and absorption properties, recreating the biomechanical heterogeneity of the natural meniscus. Consequently, the regenerated neomeniscus successfully realized chondroprotective function and attenuated cartilage degeneration. The molecular etching strategy and scaffold optimization balanced the biocompatibility and biomechanical properties of the TEM. The biomimetic GSDP-TEM achieved the synergistic effect of biomechanical and biological heterogeneities, which could also provide references for engineering other load-bearing heterogeneous tissues.

Biologically, the GSDP-TEM microtopology mediated regional-specific BMSCs differentiation. The BMSCs in the inner zone of the GSDP-TEM were mostly differentiated into chondrocyte-like cells and secreted more COL-2 and GAG, while most fibroblast-like cells and more COL-1 deposition were observed in the outer zone of the GSDP-TEM. This allowed gradient biological heterogeneity self-construction. Other studies have also recognized the importance of biological heterogeneity reconstruction, and regional-specific cytokines, decellularized ECM, etc., were employed to reconstruct biological biomimetic TEMs [10–13]. However, the gradient transitions of the natural meniscus cell phenotype, ECM deposition and fibre alignments were still not implemented, which is one of the most important parameters that affects biofunction restoration [42]. Previous studies have shown that cell behaviour and mechanical properties can be regulated by scaffold microtopology [43]. Therefore, the biomimetic microenvironment was supposed to be

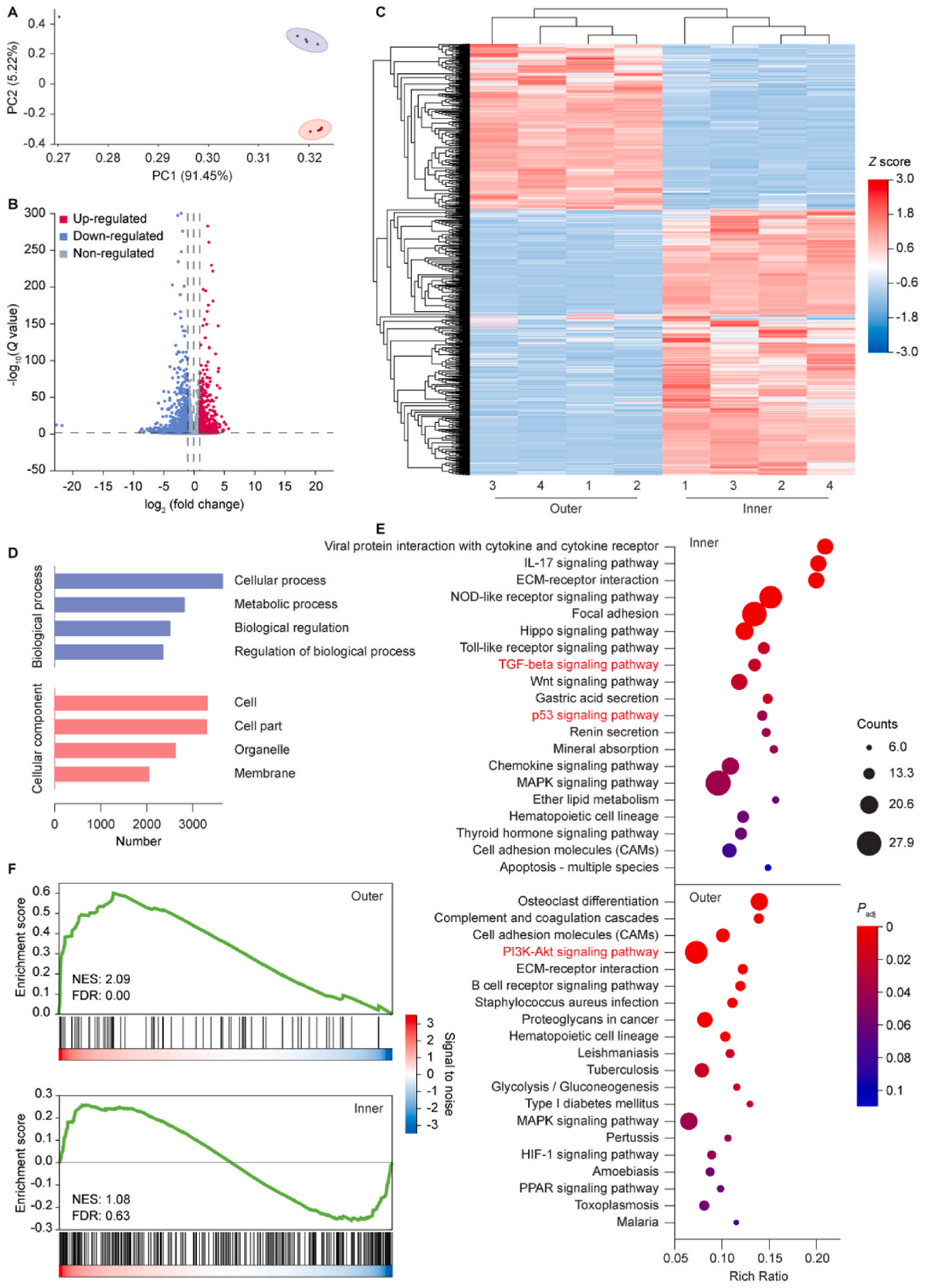

Fig. 8. The molecular mechanism of GSDP-TEM-induced construction of biological heterogeneity. A, PCA of DEGs of cells on the inner and outer zones of GSDP-TEM. **B–C**, Volcano map (**B**) and heatmap (**C**) illustrating DEGs of BMSCs grown on the inner and outer zones of GSDP-TEM. **D**, Top four biological process (BP) and cellular component (CC) GO terms enriched in DEGs (see Figure S14C for all enriched GO terms). **E**, KEGG pathway analysis of DEGs highly expressed by BMSCs in the inner zone and outer zone of GSDP-TEM. **F,** GSEA comparing the correlation between PI3K-Akt and p53 signaling pathways and highly expressed DEGs.

achieved by regulating the geometric microstructural designs of the biomaterials for 3D cell culture [44]. Notably, a larger micropore size demonstrated the potential to promote BMSCs differentiation into fibroblast-like cells, while a smaller micropore size was proven to promote chondrogenesis [45]. In our previously reported work, PCL scaffolds with 215 μm sized micropores demonstrated the best fibrocartilage tissue formation and cartilage protection effect [46]. Therefore, the GSDP-TEM of the present study was designed with a gradient-sized diamond-shaped microporous structure that possessed smaller pores on the inside and larger pores on the outside, with an average micropore size of 215 μm. The in vitro results showed that the GSDP-TEM demonstrated a regional-specific cell phenotype and ECM deposition, establishing a strong biochemical foundation for biomimetic function realization. It should be noted that BMSCs were distributed both on the surface of PCL fibres and the middle of pores (Figure S2), but the latter was inevitably removed due to the experimental operation, and the RNA sequencing was employed to collect all of the BMSCs on fibres and in pores. The microtopology effect of the GSDP-TEM was introduced here to induce biological heterogeneity regeneration, demonstrating several advantages of the GSDP-TEM in terms of controllability, simplicity and practicability and suggesting the high potential of this material in clinical applications.

In the present study, the microtopology effect produced by adjusting the micropore shape and size was used to regulate BMSCs differentiation and achieve targeted regulation. The principle of heterogeneous regulation was supposed to be related to transduction between micromechanics and chemical signals. Cell behaviours can be regulated by molecular interactions between cells and the biochemical or biomechanical microenvironment [47], and these interactions can be transformed into intracellular chemical signals [48–50]. In the present study, different micromechanical stimulations combined with cytokines regulated heterogeneous cell differentiation through changes in intracellular chemical signals. The RNA sequencing results demonstrated that the PI3K-Akt/P53 signalling pathway was enriched in the outer/inner zone of the GSDP-TEM with enhanced DEGs expression, which was reported to promote BMSCs differentiation into fibroblast-like/chondrocyte-like cells [51,52]. In addition, zone specific genes haven been reported by previous research [53–55], and *PDGFRA, LPAR2, SYK, TGFA, FGF7* were found to be upregulated in the outer zone of GSDP-TEM, while *SERPIN E1, BMP-6, BMPR* were upregulated in the inner zone in the present study. Therefore, biomimetic heterogeneities were achieved through the microtopologically induced micromechanical environment and molecular mechanism modification. However, this result only preliminarily clarified the mechanism of the microtopology-micromechanics-biochemical signal axis, and more in-depth research is needed to further confirm the biological effect of the selected DEGs. In addition, BMSCs presented the highest proliferative effect on the scaffolds with gradient-sized diamond-shaped pores. The results corresponded to previous studies suggesting that cellular behavior could be regulated by the topography or 3D geometry of scaffolds [56–58]. The diamond pores design can theoretically increase the circumferential and oblique fibers to disperse the stresses loaded onto the meniscus compared to other pore structures. Thus, diamond micropores, which are more suitable for promoting cell proliferation than square micropores, were selected for the structural design of the GSDP-TEM.

Biomechanically, the GSDP-TEM possessed excellent load transfer and absorption properties, recreating the natural biomechanical heterogeneity of the meniscus through a biomimetic mechanical architecture. The natural meniscus provides vital biomechanical functions in the knee joint [59]. Upon weight-bearing, the meniscus receives compression produced by the axial load from the knee joint and converts it into stresses along the circumferential direction [60], which allows the gradual transition of compressive into tensile stress from the inside out [61]. Mechanical properties are crucial to the development and maintenance of load-bearing TEM regeneration, including shock absorption, creep deformation, tensile and compressive properties [62,63]. However, previous studies mostly focused on the bionics of tensile or compressive modulus [64]. Load transmission and absorption are often overlooked but are closely related to the chondroprotection capacity of the meniscus. The outstanding biomechanical properties of the GSDP-TEM might be one of the reasons for the good chondroprotection results obtained after in vivo implantation.

The tissue regeneration and chondroprotection ability of the neomeniscus were successfully attained in vivo. The in vivo results showed that the GSDP-TEM induced meniscal regeneration, restored meniscal biofunctions, and alleviated OA progression, which indicated that this TEM outperformed the uniformly structured TEMs (USSP/USDP-TEM). The reason for this might be the reconstruction of the biotic mechanical environment. Articular cartilage degeneration is closely related to the mechanical microenvironment within the joint, while meniscus injury or deficiency can destroy intra-articular biomechanics and lead to joint force line offset, accelerating cartilage degeneration and OA development [2]. Recently, several meniscal substitution products were investigated in vivo, but some complications were reported after implantation, such as extrusion, nonintegration, dislocation, and OA exacerbation [65–67]. The reason for this might be the incompatible biomechanics and long-term promoting effect of tissue regeneration, while the GSDP-TEM demonstrated sequential tissue regeneration and chondroprotection ability due to the dynamic match of the natural development process. In the early stage after implantation, the excellent mechanical properties of the GSDP-TEM contributed primarily to restoring the biomechanical functions of the natural meniscus to buffer stress and protect cartilage. Subsequently, the gradient microtopology of the GSDP-TEM induced neomeniscus regeneration with biomimetic heterogeneous biological distributions under natural mechanical stress stimulation, which coordinated with the biomechanical properties of the GSDP-TEM to achieve the long-term mission of chondroprotection. Considering the objective of the present study was to investigate the effect of scaffold topology, the non-cell seeded scaffold and non-repaired meniscus control group were not involved here. In addition, our previous study has reported that cell-seeded scaffold induced better fibrocartilaginous tissue regeneration and mechanical strength than non-cell seeded scaffold and total meniscectomy group [68].

The NaOH etching protocol and high-M_w PCL material were introduced to balance the mechanical strength and cell adhesion ability, significantly improving the scaffold biocompatibility with a negligible decrease in mechanical strength. After comparing of the compressibility, stretchability, cytocompatibility of the state-of-art materials for meniscal replacement, PCL was selected to construct the scaffold in this work due to its superior mechanical properties, high biocompatibility [69], and high material processability for 3D printing [13,70], outperforming other materials (Figure S15). Besides, PCL is one of the most potential materials for clinical application in meniscal substitution, especially for high-M_w PCL, which endows the bulk material with a higher mechanical strength [71,72]. However, the negative cytocompatibility of high-M_w PCL still need to be optimized. To balance the mechanical strength and cell adhesion ability, NaOH etching method was employed to modify the hydrophobic surfaces of the high-M_w PCL scaffolds. Compared to other hydrophilic modification methods, such as protein coating, cold plasma treatment, and chemical etching, the NaOH etching method was chosen because it is more rapid, simple, inexpensive, and efficient [73]. The hydrophilicity of the 3D-printed scaffold was significantly improved with an appropriate soaking time in alkaline solution. It should be noted that the degradation rate of PCL was relatively fast, which might due to the increased surface roughness and ester bond hydrolysis caused by NaOH etching. Further research is still needed to explore more suitable concentrations and action times.

The biggest strength of the present study is realizing the synergetic effect of biological and biomechanical heterogeneities, which is crucial for functional meniscus reconstruction and serves as a great challenge in bioengineering and regenerative medicine. Previous studies realized great biological effects but not biomechanical properties [10,11,74] or

realized biomechanical properties but not biological activity [64]. Here, the vital synergetic effect of the biological and biomechanical heterogeneities of the GSDP-TEM was adequately realized by the microtopology effect, providing a solid foundation for biofunction restoration within the knee joint. GSDP-TEM generated heterogeneous Young's modulus and load distribution property, which were crucial for meniscus biofunctions realization but always overlooked by previous research [75,76]. Micro-CT analysis showed that GSDP-TEM significantly improved the condition of articular cartilage, which indicates that GSDP-TEM retard subchondral bone remodelling and alleviate the progression of OA. Such microtopology-induced functional adjustment in cell differentiation and biomechanics also provides a simple and effective solution to the challenging problem of complex heterogeneous structure reconstruction. Similar strategies could be applied to reconstruct other load-bearing tissues, including but not limited to the bone, cartilage, intervertebral disc, and cardiac system, in the future. In summary, the present study accomplishes functional meniscus reconstruction with high clinical translation potential and provides a next-generation approach for the reconstruction of functional heterogeneous tissues.

There are still some limitations and challenges in the present study that need to be considered in future studies. First, preliminary RNA-sequencing analysis was employed in the present study to identify the specific molecular mechanism of topological-induced BMSCs heterogeneous differentiation and biomechanical optimization. However, more in-depth research is needed to further confirm the induced effect of selected DEGs and related signalling pathways. Second, rabbits were selected as the most common animal model for meniscus reconstruction, but the sports model, knee joint biomechanics, anatomy and mechanical properties of meniscus are still not exactly consistent with the human body. Therefore, large animal models, such as sheep or swine models, may be more relevant in future preclinical studies.

5. Conclusion

The present study presented a novel TEM with a unique gradient-sized diamond-pored microstructure (GSDP-TEM) to mimic the heterogeneous architecture of the natural meniscus, introducing the effect of micro-topology to dually rebuild the heterogeneities and biofunctions of meniscus. The results showed that GSDP-TEM demonstrates excellent biomechanical properties and regional-specific differentiation of stem cells induced by the orchestrated microstructure. The natural biofunctions of chondroprotection was effectively restored and the progression of cartilage degeneration was attenuated. Therefore, the present study provided a new perspective of the topology-induced biomechanical and biochemical heterogeneities reconstruction, which could be promoted to the construction of multiple heterogeneous load-bearing tissues in human body with strong clinical translational potential.

Data availability statement

The data are available from the corresponding author (bysyjiangdong@126.com) on reasonable request.

Ethics approval

The protocol was complied with the Guide for the Care and Use of Laboratory Animals published by the National Academy Press (National Institutes of Health Publication No. 85-23, revised 1996), and the procedures involving animal experiments were reviewed and approved by the IRB Medical Committee of Peking University Third Hospital (grant. A2022019) and Institutional Review Board of Peking University (PUIRB-LA2022629).

All authors have contributed to this work and approved the manuscript for submission to Bioactive Materials.

CRediT authorship contribution statement

Mingze Du: Investigation, Methodology, Project administration, Writing – original draft, Writing – review & editing. **Kangze Liu:** Investigation, Methodology, Software, Writing – original draft. **Huinan Lai:** Investigation, Methodology, Project administration, Software, Writing – original draft. **Jin Qian:** Formal analysis, Supervision. **Liya Ai:** Project administration. **Jiying Zhang:** Methodology. **Jun Yin:** Conceptualization, Funding acquisition, Investigation, Project administration, Supervision, Writing – review & editing. **Dong Jiang:** Conceptualization, Funding acquisition, Project administration, Supervision, Validation, Writing – review & editing.

Declaration of competing interest

The authors declare that they have no known competing financial interests or personal relationships that could have appeared to influence the work reported in this paper.

Acknowledgments

We thank Y.F. Jiang from the Peking University Third Hospital for help with statistical analysis. We thank the Peking University Medical and Health Analysis Center. This work was supported by National Key R&D Program of China (No. 2019YFB1706905), National Natural Science Foundation of China (82072428, 52075482) and Natural Science Foundation of Beijing, China (7212132).

Appendix A. Supplementary data

Supplementary data to this article can be found online at https://doi.org/10.1016/j.bioactmat.2024.03.005.

References

[1] B. Berg, E.M. Roos, M. Englund, N.J. Kise, A. Tiulpin, S. Saarakkala, L. Engebretsen, C.N. Eftang, I. Holm, M.A. Risberg, Development of osteoarthritis in patients with degenerative meniscal tears treated with exercise therapy or surgery: a randomized controlled trial, Osteoarthritis Cartilage 28 (7) (2020) 897–906.

[2] J.L. Whittaker, J.M. Losciale, C.B. Juhl, J.B. Thorlund, M. Lundberg, L.K. Truong, M. Miciak, B.L. van Meer, A.G. Culvenor, K.M. Crossley, E.M. Roos, S. Lohmander, M. van Middelkoop, Risk factors for knee osteoarthritis after traumatic knee injury: a systematic review and meta-analysis of randomised controlled trials and cohort studies for the OPTIKNEE Consensus, Br. J. Sports Med. 56 (24) (2022) 1406–1421.

[3] E.K. Danso, J.T.J. Honkanen, S. Saarakkala, R.K. Korhonen, Comparison of nonlinear mechanical properties of bovine articular cartilage and meniscus, J. Biomech. 47 (1) (2014) 200–206.

[4] B. Bilgen, C.T. Jayasuriya, B.D. Owens, Current concepts in meniscus tissue engineering and repair, Adv. Healthcare Mater. 7 (11) (2018) 1701407.

[5] L.S. Lohmander, P.M. Englund, L.L. Dahl, E.M. Roos, The long-term consequence of anterior cruciate ligament and meniscus injuries: osteoarthritis, Am. J. Sports Med. 35 (10) (2007) 1756–1769.

[6] H. Kwon, W.E. Brown, C.A. Lee, D. Wang, N. Paschos, J.C. Hu, K.A. Athanasiou, Surgical and tissue engineering strategies for articular cartilage and meniscus repair, Nat. Rev. Rheumatol. 15 (9) (2019) 550–570.

[7] E. Losina, A.D. Paltiel, A.M. Weinstein, E. Yelin, D.J. Hunter, S.P. Chen, K. Klara, L. G. Suter, D.H. Solomon, S.A. Burbine, Lifetime medical costs of knee osteoarthritis management in the United States: impact of extending indications for total knee arthroplasty, Arthritis Care Res. 67 (2) (2015) 203–215.

[8] K.A. Athanasiou, J. Sanchez-Adams, Engineering the knee meniscus, Synthesis Lectures on Tissue Eng. 1 (1) (2009) 1–97.

[9] C.J. Moran, A. Busilacchi, C.A. Lee, K.A. Athanasiou, P.C. Verdonk, Biological augmentation and tissue engineering approaches in meniscus surgery, Arthrosc. J. Arthrosc. Relat. Surg. 31 (5) (2015) 944–955.

[10] W. Guo, M. Chen, Z. Wang, Y. Tian, J. Zheng, S. Gao, Y. Li, Y. Zheng, X. Li, J. Huang, 3D-printed cell-free PCL–MECM scaffold with biomimetic microstructure and micro-environment to enhance in situ meniscus regeneration, Bioact. Mater. 6 (10) (2021) 3620–3633.

[11] L. Hao, Z. Tianyuan, Y. Zhen, C. Fuyang, W. Jiang, Y. Zineng, D. Zhengang, L. Shuyun, H. Chunxiang, Y. Zhiguo, Biofabrication of cell-free dual drug-releasing biomimetic scaffolds for meniscal regeneration, Biofabrication 14 (1) (2021) 015001.

[12] M.L. Terpstra, J. Li, A. Mensinga, M. de Ruijter, M.H.P. van Rijen, C. Androulidakis, C. Galiotis, I. Papantoniou, M. Matsusaki, J. Malda, Bioink with cartilage-derived

extracellular matrix microfibers enables spatial control of vascular capillary formation in bioprinted constructs, Biofabrication 14 (3) (2022) 034104.
[13] Z.-Z. Zhang, Y.-R. Chen, S.-J. Wang, F. Zhao, X.-G. Wang, F. Yang, J.-J. Shi, Z.-G. Ge, W.-Y. Ding, Y.-C. Yang, Orchestrated biomechanical, structural, and biochemical stimuli for engineering anisotropic meniscus, Sci. Transl. Med. 11 (487) (2019) eaao0750.
[14] Z.Z. Zhang, W.M. Guo, S. Gao, M.X. Chen, X. Li, X.L. Zhang, X.G. Jing, M.J. Wang, Y. Zhang, S. Shen, Z.H. Wang, B.C. Sun, Y. Chai, C.F. Zhou, S.Y. Liu, Q.Y. Guo, Native tissue-based strategies for meniscus repair and regeneration, Cell Tissue Res. 373 (2) (2018) 337–350.
[15] G. Conoscenti, T. Schneider, K. Stoelzel, F.C. Pavia, V. Brucato, C. Goegele, V. La Carrubba, G. Schulze-Tanzil, PLLA scaffolds produced by thermally induced phase separation (TIPS) allow human chondrocyte growth and extracellular matrix formation dependent on pore size, Mater. Sci. Eng., C 80 (2017) 449–459.
[16] S.W. Li, F. Tallia, A.A. Mohammed, M.M. Stevens, J.R. Jones, Scaffold channel size influences stem cell differentiation pathway in 3-D printed silica hybrid scaffolds for cartilage regeneration, Biomater. Sci. 8 (16) (2020) 4458–4466.
[17] Q. Zhang, H.X. Lu, N. Kawazoe, G.P. Chen, Pore size effect of collagen scaffolds on cartilage regeneration, Acta Biomater. 10 (5) (2014) 2005–2013.
[18] E.M. Byrne, E. Farrell, L.A. McMahon, M.G. Haugh, F.J. O'Brien, V.A. Campbell, P. J. Prendergast, B.C. O'Connell, Gene expression by marrow stromal cells in a porous collagen-glycosaminoglycan scaffold is affected by pore size and mechanical stimulation, J. Mater. Sci. Mater. Med. 19 (11) (2008) 3455–3463.
[19] J. Rnjak-Kovacina, S.G. Wise, Z. Li, P.K.M. Maitz, C.J. Young, Y.W. Wang, A. S. Weiss, Tailoring the porosity and pore size of electrospun synthetic human elastin scaffolds for dermal tissue engineering, Biomaterials 32 (28) (2011) 6729–6736.
[20] M.C. McNamara, F. Sharifi, A.H. Wrede, D.F. Kimlinger, D.G. Thomas, J.B. Vander Wiel, Y.F. Chen, R. Montazami, N.N. Hashemi, Microfibers as physiologically relevant platforms for creation of 3D cell cultures, Macromol. Biosci. 17 (12) (2017).
[21] B. Rentsch, A. Hofmann, A. Breier, C. Rentsch, D. Scharnweber, Embroidered and surface modified polycaprolactone-Co-lactide scaffolds as bone substitute: in vitro characterization, Ann. Biomed. Eng. 37 (10) (2009) 2118–2128.
[22] Z.-X. Zhou, Y.-R. Chen, J.-Y. Zhang, D. Jiang, F.-Z. Yuan, Z.-M. Mao, F. Yang, W.-B. Jiang, X. Wang, J.-K. Yu, Facile strategy on hydrophilic modification of poly (ε-caprolactone) scaffolds for assisting tissue-engineered meniscus constructs in vitro, Front. Pharmacol. 11 (471) (2020).
[23] X.D. Ju, M. Deng, Y.F. Ao, C.L. Yu, J.Q. Wang, J.K. Yu, G.Q. Cui, Y.L. Hu, The protective effect of tetramethylpyrazine on cartilage explants and chondrocytes, J. Ethnopharmacol. 132 (2) (2010) 414–420.
[24] G.C. Ding, X.P. Li, M.Y. Sun, Y.Y. He, F.Y. Zhao, T. Wu, J.Y. Wang, S. Ren, W.L. Shi, L.Z. Xu, X.Q. Hu, W. Huang, R. Yu, Y.F. Ao, Meniscal transplantation and regeneration using functionalized polyurethane bionic scaffold and digital light processing 3D printing, Chem. Eng. J. 431 (2022).
[25] D. Jiang, L.-H. Zhao, M. Tian, J.-Y. Zhang, J.-K. Yu, Meniscus transplantation using treated xenogeneic meniscal tissue: viability and chondroprotection study in rabbits, Arthrosc. J. Arthrosc. Relat. Surg. 28 (8) (2012) 1147–1159.
[26] E. Kon, C. Chiari, M. Marcacci, M. Delcogliano, D.M. Salter, I. Martin, L. Ambrosio, M. Fini, M. Tschon, E. Tognana, Tissue engineering for total meniscal substitution: animal study in sheep model, Tissue Eng. 14 (6) (2008) 1067–1080.
[27] L. Li, L. Yang, K. Zhang, L. Zhu, X. Wang, Q. Jiang, Three-dimensional finite-element analysis of aggravating medial meniscus tears on knee osteoarthritis, J. Orthopaedic Translat. 20 (2020) 47–55.
[28] A.E. Kedgley, T.-H. Saw, N.A. Segal, U.N. Hansen, A.M.J. Bull, S.D. Masouros, Predicting meniscal tear stability across knee-joint flexion using finite-element analysis, Knee Surg. Sports Traumatol. Arthrosc. 27 (1) (2019) 206–214.
[29] E. Kon, G. Filardo, M. Tschon, M. Fini, G. Giavaresi, L.M. Reggiani, C. Chiari, S. Nehrer, I. Martin, D.M. Salter, Tissue engineering for total meniscal substitution: animal study in sheep model—results at 12 months, Tissue Eng. 18 (15–16) (2012) 1573–1582.
[30] C.G. Peterfy, A. Guermazi, S. Zaim, P.F.J. Tirman, Y. Miaux, D. White, M. Kothari, Y. Lu, K. Fye, S. Zhao, Whole-organ magnetic resonance imaging score (WORMS) of the knee in osteoarthritis, Osteoarthritis Cartilage 12 (3) (2004) 177–190.
[31] M. Brittberg, C.S. Winalski, Evaluation of cartilage injuries and repair, JBJS 85 (suppl_2) (2003) 58–69.
[32] A.J. Fox, F. Wanivenhaus, A.J. Burge, R.F. Warren, S.A. Rodeo, The Human Meniscus, 2015.
[33] Z. Cui, J. Crane, H. Xie, X. Jin, G. Zhen, C. Li, L. Xie, L. Wang, Q. Bian, T. Qiu, Halofuginone attenuates osteoarthritis by inhibition of TGF-β activity and H-type vessel formation in subchondral bone, Ann. Rheum. Dis. 75 (9) (2016) 1714–1721.
[34] G.C.J. Brown, K.S. Lim, B.L. Farrugia, G.J. Hooper, T.B.F. Woodfield, Covalent incorporation of heparin improves chondrogenesis in photocurable gelatin-methacryloyl hydrogels, Macromol. Biosci. 17 (12) (2017).
[35] T. Dehne, R. Schenk, C. Perka, L. Morawietz, A. Pruss, M. Sittinger, C. Kaps, J. Ringe, Gene expression profiling of primary human articular chondrocytes in high-density micromasses reveals patterns of recovery, maintenance, re- and dedifferentiation, Gene 462 (1–2) (2010) 8–17.
[36] E. Geervliet, L. Terstappen, R. Bansal, Hepatocyte survival and proliferation by fibroblast growth factor 7 attenuates liver inflammation, and fibrogenesis during acute liver injury via paracrine mechanisms, Biomed. Pharmacother. 167 (2023).
[37] L.S. Huang, P.F. Fu, P. Patel, A. Harijith, T.J. Sun, Y.T. Zhao, J.G.N. Garcia, J. Chun, V. Natarajan, Lysophosphatidic acid receptor-2 deficiency confers protection against bleomycin-induced lung injury and fibrosis in mice, Am. J. Respir. Cell Mol. Biol. 49 (6) (2013) 912–922.
[38] C. Qu, D.D. Zheng, S. Li, Y.J. Liu, A. Lidofsky, J.A. Holmes, J.N. Chen, L. He, L. Wei, Y.D. Liao, H. Yuan, Q.M. Jin, Z.L. Lin, Q.T. Hu, Y.C. Jiang, M.X. Tu, X.J. Chen, W. M. Li, W.Y. Lin, B.C. Fuchs, R.T. Chung, J. Hong, Tyrosine kinase SYK is a potential therapeutic target for liver fibrosis, Hepatology 68 (3) (2018) 1125–1139.
[39] B.O. Diekman, B.T. Estes, F. Guilak, The effects of BMP6 overexpression on adipose stem cell chondrogenesis: interactions with dexamethasone and exogenous growth factors, J. Biomed. Mater. Res. 93A (3) (2010) 994–1003.
[40] P.T. Lee, W.J. Li, Chondrogenesis of embryonic stem cell-derived mesenchymal stem cells induced by TGF1 and BMP7 through increased TGF receptor expression and endogenous TGF1 production, J. Cell. Biochem. 118 (1) (2017) 172–181.
[41] B.S. Yoon, D.A. Ovchinnikov, I. Yoshii, Y. Mishina, R.R. Behringer, K.M. Lyons, *Bmpr1a* and *Bmpr1b* have overlapping functions and are essential for chondrogenesis <i>in vivo</i&gt, Proc. Natl. Acad. Sci. U.S.A. 102 (14) (2005) 5062–5067.
[42] H. Sun, X. Wen, H. Li, P. Wu, M. Gu, X. Zhao, Z. Zhang, S. Hu, G. Mao, R. Ma, W. Liao, Z. Zhang, Single-cell RNA-seq analysis identifies meniscus progenitors and reveals the progression of meniscus degeneration, Ann. Rheum. Dis. 79 (3) (2019) 408–417.
[43] F.R. Noyes, S.D. Barber-Westin, Repair of complex and avascular meniscal tears and meniscal transplantation, JBJS 92 (4) (2010) 1012–1029.
[44] M. Bao, J. Xie, A. Piruska, W.T. Huck, 3D microniches reveal the importance of cell size and shape, Nat. Commun. 8 (1) (2017) 1–12.
[45] Q. Zhang, H. Lu, N. Kawazoe, G. Chen, Pore size effect of collagen scaffolds on cartilage regeneration, Acta Biomater. 10 (5) (2014) 2005–2013.
[46] Z.-Z. Zhang, D. Jiang, J.-X. Ding, S.-J. Wang, L. Zhang, J.-Y. Zhang, Y.-S. Qi, X.-S. Chen, J.-K. Yu, Role of scaffold mean pore size in meniscus regeneration, Acta Biomater. 43 (2016) 314–326.
[47] J.A. Hubbell, M.P. Lutolf, Synthetic biomaterials as instructive extracellular microenvironments for morphogenesis in tissue engineering, Nat. Biotechnol. 23 (1) (2005) 47–55.
[48] B.M. Baker, B. Trappmann, W.Y. Wang, M.S. Sakar, I.L. Kim, V.B. Shenoy, J. A. Burdick, C.S. Chen, Cell-mediated fibre recruitment drives extracellular matrix mechanosensing in engineered fibrillar microenvironments, Nat. Mater. 14 (12) (2015) 1262–1268.
[49] M.L. Cagigas, N.S. Bryce, N. Ariotti, S. Brayford, P.W. Gunning, E.C. Hardeman, Correlative cryo-ET identifies actin/tropomyosin filaments that mediate cell–substrate adhesion in cancer cells and mechanosensitivity of cell proliferation, Nat. Mater. 21 (1) (2022) 120–128.
[50] S. Jiang, C. Lyu, P. Zhao, W. Li, W. Kong, C. Huang, G.M. Genin, Y. Du, Cryoprotectant enables structural control of porous scaffolds for exploration of cellular mechano-responsiveness in 3D, Nat. Commun. 10 (1) (2019), 3491-14.
[51] S.U. Hettiarachchi, Y.-H. Li, J. Roy, F. Zhang, E. Puchulu-Campanella, S. D. Lindeman, M. Srinivasarao, K. Tsoyi, X. Liang, E.A. Ayaub, Targeted inhibition of PI3 kinase/mTOR specifically in fibrotic lung fibroblasts suppresses pulmonary fibrosis in experimental models, Sci. Transl. Med. 12 (567) (2020) eaay3724.
[52] T.G. Zhang, X.D. Li, G.Y. Yu, P. Xie, Y.G. Wang, Z.Y. Liu, Q. Hong, D.Z. Liu, S.X. Du, All-trans-retinoic acid inhibits chondrogenesis of rat embryo hindlimb bud mesenchymal cells by downregulating p53 expression, Mol. Med. Rep. 12 (1) (2015) 210–218.
[53] W.L. Fu, S.J. Chen, R.Z. Yang, C. Li, H.X. Gao, J. Li, X.G. Zhang, Cellular features of localized microenvironments in human meniscal degeneration: a single-cell transcriptomic study, Elife 11 (2022).
[54] H. Sun, X.Z. Wen, H.Y. Li, P.H. Wu, M.H. Gu, X.Y. Zhao, Z.J. Zhang, S. Hu, G. P. Mao, R.F. Ma, W.M. Liao, Z.Q. Zhang, Single-cell RNA-seq analysis identifies meniscus progenitors and reveals the progression of meniscus degeneration, Ann. Rheum. Dis. 79 (3) (2020) 408–417.
[55] H. Sun, W.H. Zhang, F.Z. Liu, D. Li, Z.Q. Cai, Z.C. Huang, M.Y. Chen, Z.C. Lin, J. Xu, R.F. Ma, Single-cell RNA sequencing reveals the cell types heterogenicity of human discoid lateral meniscus cells, J. Cell. Physiol. 237 (5) (2022) 2469–2477.
[56] F. Causa, P.A. Netti, L. Ambrosio, A multi-functional scaffold for tissue regeneration: the need to engineer a tissue analogue, Biomaterials 28 (34) (2007) 5093–5099.
[57] M.C. Chen, Y.C. Sun, Y.H. Chen, Electrically conductive nanofibers with highly oriented structures and their potential application in skeletal muscle tissue engineering, Acta Biomater. 9 (3) (2013) 5562–5572.
[58] J.M. Singelyn, J.A. DeQuach, S.B. Seif-Naraghi, R.B. Littlefield, P.J. Schup-Magoffin, K.L. Christman, Naturally derived myocardial matrix as an injectable scaffold for cardiac tissue engineering, Biomaterials 30 (29) (2009) 5409–5416.
[59] J. Buckwalter, Articular Cartilage: Injury and Repair, Injury and Repair of the Musculoskeletal Soft Tissues, 1987, pp. 465–482.
[60] T. Hirose, T. Mae, I. Ogasawara, S. Yamakawa, K. Nakata, T. Ohori, A. Tsujii, S. Okada, Meniscal displacement and loss of load-transmission function after radial tear of the lateral meniscus in a porcine model: new insights into the functional dynamics of the injured meniscus, Am. J. Sports Med. 50 (7) (2022) 1850–1857.
[61] M.A. LeRoux, Biphasic finite element modeling of tear effects on the mechanics of the meniscus, in: ASME Summer Bioengineering Conference, vol. 2001, 2001, pp. 851–852.
[62] M. Chen, W. Guo, S. Gao, C. Hao, S. Shen, Z. Zhang, Z. Wang, X. Li, X. Jing, X. Zhang, Z. Yuan, M. Wang, Y. Zhang, J. Peng, A. Wang, Y. Wang, S. Xiang, S. Liu, Q. Guo, Biomechanical stimulus based strategies for meniscus tissue engineering and regeneration, Tissue engineering, Part B, Reviews 24 (ja) (2018) 392–402.
[63] S.E. Szczesny, C.S. Lee, L.J. Soslowsky, Remodeling and repair of orthopedic tissue: role of mechanical loading and biologics, Am. J. Orthoped. 39 (11) (2010) 525–530.

[64] Y. Yang, Z. Chen, X. Song, Z. Zhang, J. Zhang, K.K. Shung, Q. Zhou, Y. Chen, Biomimetic anisotropic reinforcement architectures by electrically assisted nanocomposite 3D printing, Adv. Mater. 29 (11) (2017) 1605750–n/a.
[65] D.A. Houck, M.J. Kraeutler, J.W. Belk, E.C. McCarty, J.T. Bravman, Similar clinical outcomes following collagen or polyurethane meniscal scaffold implantation: a systematic review, Knee Surg. Sports Traumatol. Arthrosc. : Off. J. ESSKA 26 (8) (2018) 2259–2269.
[66] R. Papalia, F. Franceschi, L.D. Balzani, S. D'Adamio, N. Maffulli, V. Denaro, Scaffolds for partial meniscal replacement: an updated systematic review, Br. Med. Bull. 107 (1) (2013) 19–40.
[67] C.D.S. Ranmuthu, C.K.I. Ranmuthu, J.C. Russell, D. Singhania, W.S. Khan, Are the biological and biomechanical properties of meniscal scaffolds reflected in clinical practice? A systematic review of the literature, Int. J. Mol. Sci. 20 (3) (2019) 632.
[68] Z.-Z. Zhang, S.-J. Wang, J.-Y. Zhang, W.-B. Jiang, A.-B. Huang, Y.-S. Qi, J.-X. Ding, X.-S. Chen, D. Jiang, J.-K. Yu, 3D-printed poly (ε-caprolactone) scaffold augmented with mesenchymal stem cells for total meniscal substitution: a 12-and 24-week animal study in a rabbit model, Am. J. Sports Med. 45 (7) (2017) 1497–1511.
[69] H. Kweon, M.K. Yoo, I.K. Park, T.H. Kim, H.C. Lee, H.-S. Lee, J.-S. Oh, T. Akaike, C.-S. Cho, A novel degradable polycaprolactone networks for tissue engineering, Biomaterials 24 (5) (2003) 801–808.
[70] E.A. Makris, P. Hadidi, K.A. Athanasiou, The knee meniscus: structure–function, pathophysiology, current repair techniques, and prospects for regeneration, Biomaterials 32 (30) (2011) 7411–7431.
[71] A.D. Olubamiji, Z. Izadifar, J.L. Si, D.M.L. Cooper, B.F. Eames, D.X.B. Chen, Modulating mechanical behaviour of 3D-printed cartilage-mimetic PCL scaffolds: influence of molecular weight and pore geometry, Biofabrication 8 (2) (2016) 025020.
[72] H. Sun, L. Mei, C. Song, X. Cui, P. Wang, The in vivo degradation, absorption and excretion of PCL-based implant, Biomaterials 27 (9) (2006) 1735–1740.
[73] Z. Ma, Z. Mao, C. Gao, Surface modification and property analysis of biomedical polymers used for tissue engineering, Colloids Surf. B Biointerfaces 60 (2) (2007) 137–157.
[74] M.L. Terpstra, J. Li, A. Mensinga, M. de Ruijter, M.H.P. van Rijen, C. Androulidakis, C. Galiotis, I. Papantoniou, M. Matsusaki, J. Malda, R. Levato, Bioink with cartilage-derived extracellular matrix microfibers enables spatial control of vascular capillary formation in bioprinted constructs, Biofabrication 14 (3) (2022).
[75] C.H. Lee, S.A. Rodeo, L.A. Fortier, C.Y. Lu, C. Erisken, J.J. Mao, Protein-releasing polymeric scaffolds induce fibrochondrocytic differentiation of endogenous cells for knee meniscus regeneration in sheep, Sci. Transl. Med. 6 (266) (2014).
[76] H. Li, Z.Y. Liao, Z. Yang, C.J. Gao, L.W. Fu, P.X. Li, T.Y. Zhao, F.Y. Cao, W. Chen, Z. G. Yuan, X. Sui, S.Y. Liu, Q.Y. Guo, 3D printed poly(epsilon-caprolactone)/meniscus extracellular matrix composite scaffold functionalized with kartogenin-releasing PLGA microspheres for meniscus tissue engineering, Front. Bioeng. Biotechnol. 9 (2021).